JM PAPERS

Insights into instability modes of supersonic square jets

Aatresh Karnam[1] [ORCID], **Myeonghwan Ahn,**[2] **Mihai Mihaescu,**[2] **Mohammad Saleem**[1] **and Ephraim Gutmark**[1]

[1]Department of Aerospace Engineering and Engineering Mechanics, University of Cincinnati, Cincinnati, USA

[2]Department of Engineering Mechanics, KTH Royal Institute of Technology, FLOW, Stockholm, Sweden

Corresponding author: Aatresh Karnam, karnamah@mail.uc.edu

The study examines supersonic square jets in a twin nozzle configuration with the aim of identifying and characterising emergent instability modes during overexpanded operation. Unlike screeching rectangular jets that undergo strong fluctuations normal to the wider jet dimension, the equilateral nature of the exit geometry in square nozzles leads to multiple instability states dictated by shock–turbulence interactions and nozzle operating conditions. Furthermore, strong coupling modes between the jets were identified that led to either phase locked or out of phase interactions of the inner shear layers. Results from experimental studies were examined using spatial and temporal decomposition techniques based on spectral methods to identify the resultants from triadic shock–turbulence interactions. The primary instability mode across both operating conditions were driven by optimal interactions while the harmonics were found to be associated with the suboptimal shock–turbulence interactions.

Key words: supersonic flow, jet noise, shear layer turbulence

1. Introduction

Non-circular nozzle geometries, especially rectangular nozzles, have garnered consistent research interest due to various advantages. They offer simplified airframe integration and thrust vector designs for dry and afterburning operation as discussed by Dusa *et al.* (1983). This interest, coupled with the need to identify behavioural traits emerging from flow

instabilities encountered in the overexpanded state of supersonic operation, has resulted in a vast body of research into these nozzles. While investigations into elliptical nozzles have been undertaken as shown by the work of Edgington-Mitchell *et al.* (2013), Edgington-Mitchell *et al.* (2022), Edgington-Mitchell, Honnery & Soria (2015) and Bell *et al.* (2018), the primary research focus in this field has been centred on the rectangular convergent–divergent (C-D) nozzles. Both single and multijet configurations spanning a wide spectrum of nozzle aspect ratios(ARs) have been investigated. The AR is commonly expressed as the ratio of nozzle length (*l*) to width (*w*) ($AR = l/w$).

Alkislar, Krothapalli & Lourenco (2003) examined the influence of screech on flow development in an underexpanded AR 4 rectangular jet and found it to be a primary contributor to axis switching through the deformation of large-scale spanwise coherent vortices. Furthermore, they identified that the spanwise location of these coherent vortices aligned with the acoustic sources resulting from strong flow fluctuations. The computational studies by Gojon, Gutmark & Mihaescu (2019) and Wu, Lele & Jeun (2023) examined screech-driven instability behaviour in AR 2 and AR 4 rectangular nozzles, respectively, and found evidence for the internal guided jet mode (G-JM) as being the primary closure mechanism for screech. The results from both studies align with the well-accepted concept of neutral internal wave modes being a means of instability closure as proposed by Shen & Tam (2002) and Manning & Lele (2000) for circular jets. Studies by Edgington-Mitchell *et al.* (2021, 2022) have conclusively proved the emergence of shock leakage, acoustic emission and the G-JM as the three resultants from triadic interactions between Kelvin–Helmholtz (*KH*) instability waves and the jet shock cells. Karnam, Saleem & Gutmark (2023) documented these interaction components emerging from screeching AR 2 rectangular jets undergoing single mode and multimode screech instabilities. Their study identified that energy allocation between the three resultants can be variable. This can lead to scenarios where shock leakage can dominate the resultant spatial energy spectrum and act as the primary closure mechanism for nozzles with large amplitude screech oscillations. The computational studies by Liang *et al.* (2023) on an AR 2, AR 5 and planar jets also showed evidence for G-JM being the primary screech closure mechanism. Furthermore, evidence of G-JM driven screech instability at higher temperature ratios (TR) was found in the AR 2 rectangular jet at TR 7 by Chen, Gojon & Mihaescu (2021).

Extensive research has also been conducted into examining the instability behaviour of large AR nozzles as described by the research summary of Raman (1999). Preliminary characterisation studies by Krothapalli *et al.* (1981, 1986) conducted on several large AR nozzles ($AR > 5$) examined rectangular jets from a finite two-dimensional flow perspective. They studied the impact of streamwise flow instabilities on the development of the jet potential core and identified that the half-velocity point ($u = 0.5U_{exit}$) of the jet varies linearly with axial distance, with slopes of the half-velocity point locus directly being a function of the nozzle AR. Semlitsch *et al.* (2020) identified the generation of shock leakage as a component emerging from screech instabilities in AR 9 rectangular jets. They concluded that this phenomenon acts as one of the closure mechanisms in the production of screech harmonics. In the context of twin nozzle flows, Raman & Taghavi (1998),Raman & Rice (1994) identified various coupling modes in AR 5 twin rectangular jets that varied as a function of the exit Mach number and internozzle spacing. The near-field acoustic measurements from their experiments indicated that the primary inter jet coupling mode exhibited antisymmetric phase behaviour while the secondary coupling mode led to symmetric phase distribution. Their studies concluded that coupling modes were sensitive to the internozzle spacing, the nozzle exit geometry and the cant angle between the nozzles. Recent research conducted by Jeun *et al.* (2022*a*,*b*) has shed light on

the screech modes in AR 2 twin rectangular jets, demonstrating that the screech closure mechanism in one nozzle remains unaffected by acoustic emissions from its counterpart. A vast body of research also exists towards understanding the behaviour of twin circular nozzles. Some notable studies include the experimental studies by Kuo *et al.* (2015, 2017), Knast *et al.* (2018) and Bell *et al.* (2021) that examined the coupling modes in C-D and pure convergent circular nozzles, respectively. Additionally, numerical studies by Ahn, Lee & Mihaescu (2021) and Montero *et al.* (2023), have utilised simulation techniques such as large-eddy simulation (LES) (Ahn *et al.* 2021*a*) and Reynold's-averaged numerical simulations (Padilla Montero *et al.* 2023), to understand the effect of nozzle spacing on jet coupling modes (Ahn *et al.* 2021*b*) and the variations in the flow development across the inner and outer shear layers (Padilla Montero *et al.* 2023), respectively. While, Rodriguez *et al.* (2023) and Stavropoulos *et al.* (2024) utilised implementations of linear stability theory (Rodríguez *et al.* 2023) and planar vortex sheet model (Stavropoulos *et al.* 2024) to predict the dominant modes in turbulent mixing regions that influence mode coupling and identify modal variations and frequency response of merging round twin planar jets, respectively.

The current study discusses findings on instability characteristics of the lesser documented square twin-nozzle configuration. Unlike circular nozzles, which generate axisymmetric shock systems due to the circular exit area, the four-way symmetry of square nozzles generates unique coupling modes not observed in twin rectangular nozzles (Jeun *et al.* 2022). Additionally, in the realm of supersonic flows, square nozzles present advantages for improved packaging for large multinozzle systems. The seminal experimental work of Zilz & Wlezien (1990) first identified the various oscillation modes observed in twin square nozzles at supersonic exit conditions featuring a single set of C-D walls. They highlighted the presence of lateral oscillation modes where the jets fluctuate in the plane parallel to the C-D walls. This is unlike the behaviour observed in rectangular jets where the oscillations occur in the plane perpendicular to the C-D walls. Notably, they observed changes in the mode behaviour relative to the internozzle spacing with the jets switching between lateral symmetric (mirror symmetry) and antisymmetric oscillation modes with increasing nozzle spacing.

Mohanta & Sridhar (2017) investigated the development of circular, square and hexagonal supersonic jets, finding that axial velocity decay was most pronounced in square jets. This behaviour was attributed to the generation of high helicity at the corners of the square jet. Nguyen, Maher & Hassan (2020) examined the flow characteristics of underexpanded supersonic square jets and investigated variations in shock structures when these jets interacted with angled surfaces. Zhang *et al.* (2015, 2017) employed LES to offer valuable insights into the complex shock structures of underexpanded flow from square jets. Their findings revealed intricate interactions between shock structures and the primary vortex ring formed during flow initiation at two underexpanded conditions. They also observed that azimuthal curvature discrepancies inherent to square nozzles caused Biot–Savart deformations in the primary vortex loop, leading to the generation of counter-rotating vortex pairs at the corners, which subsequently accelerated axis switching.

While these studies shed light on the characteristics of stable square jets, there remains a significant gap in understanding the behaviour of unstable square supersonic jets, particularly in both single and twin nozzle configurations. This study aims to develop a deeper understanding of the various unstable states of twin square supersonic jets resulting from flow driven instabilities.

To obtain a comprehensive understanding of the flow behaviour, a multifaceted data analysis approach was adopted. This involved analysing far-field acoustic data
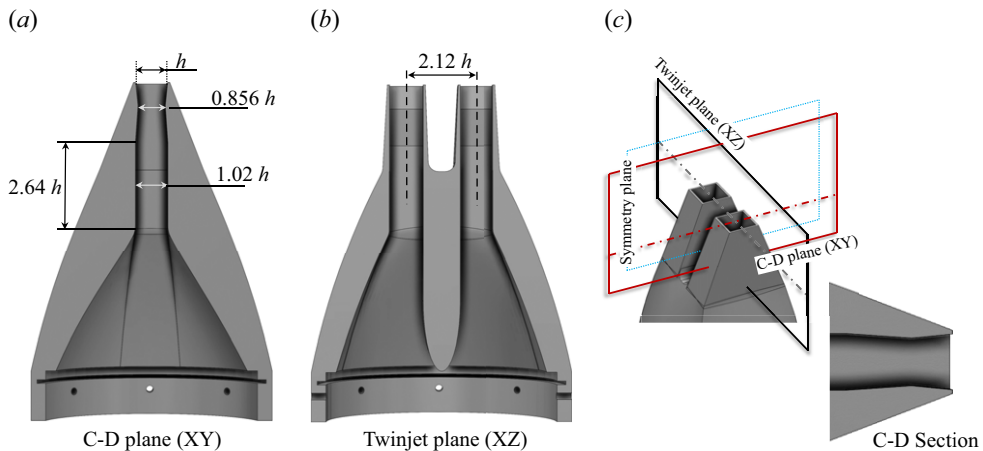
Figure 1. Profile views of the twin square nozzle. (*a*) The C-D plane: plane passing through the centre line of the C–D size of the nozzle. (*b*) Twinjet plane: plane passing through the centre lines of the two jets. (*c*) Orientation of observation planes with respect to the nozzle, clear view of the C-D section. Note that the far-field acoustics were obtained from the Symmetry plane (cyan) and not the C-D plane (red). Internozzle spacing (*s*, between nozzle inner walls) = 1.1*h*.

to characterise instability noise propagation, examining variations in the flow's shock structure through high-speed schlieren imaging, and quantifying flow statistics such as velocity and turbulence distribution using particle image velocimetry (PIV). Furthermore, temporal and spatial Fourier decomposition techniques were applied for dominant mode isolation and source identification.

2. Experimental methodology

The experimental investigations were conducted at the Aeroacoustics High Temperature Facility (AHTF), situated within the Gas Dynamics and Propulsion Laboratory at the University of Cincinnati. Acoustic and flow visualisation experiments were conducted at nozzle pressure ratios (NPR) of 2.6 and 3, at a total TR of 1 (i.e. $T_{inlet} = T_{ambient}$). The nozzle and observation planes used in the experiments are illustrated in figure 1. It consisted of two square nozzles with an exit height (*h*) of 16.61 mm. Air enters a common flow plenum (diameter = 6.61*h*) at the nozzle base and bifurcates it into two distinct and identical flow streams. Stream diversion and separation was achieved through a dividing wall profiled from a fifth-order polynomial ogive to prevent flow separation. The individual streams pass through a straight section with a square cross-section followed by a pair of C-D sections (top and bottom) with flat lateral walls to accelerate the flow to supersonic exit conditions. Each nozzle was designed to have an exit-to-throat area ratio of 1.17 leading to a design Mach number of 1.5 achieved at NPR 3.67 with identical mass flow rate delivered across both nozzles. Far field acoustic measurements were recorded using a semicircular array consisting of 16 Brüel & Kjær free field microphones placed at a radial distance of 1.12 m ($\approx$67.2*h*). The centre of curvature of the array was located at the midpoint between the nozzles. Pressure data was recorded for a period of two seconds at an acquisition rate of 204.8 kHz resulting in a total of 409600 samples. A fast Fourier transform method was implemented with a block size of 4096 samples per block resulting in a frequency resolution of 50 Hz. The computed frequency power spectrum was normalised using the standard reference pressure of 20 µPa to obtain the sound

Acquisition frequency (F_1)	41 kHz
Acquisition frequency (F_2)	112 kHz
Exposure time	10 µs
Field of view ($l \times w$)	$10h \times 9h$
No. of samples	2000

Table 1. Schlieren imaging parameters.

pressure level (SPL). The overall SPL (OASPL) was computed using a frequency integral method starting at the chamber cutoff frequency of 300 Hz to avoid capturing the reflected sound waves that can occur below this frequency. The frequencies were normalised to the Strouhal scale (St) using the equivalent diameter ($D_e = 1.30(bh)^{0.625}/(b + h)^{0.25}$; h, height; b, breadth) of a single nozzle where $D_e = 1.11h$.

A single mirror schlieren imaging technique was utilised to capture flow fluctuations from the nozzle using a Phantom v1610 high-speed camera. This technique offers increased sensitivity when compared with traditional Z-type schlieren technique due to the retraced light path to and from the mirror (Settles 2001). Table 1 details the image acquisition rate and flow field dimensions. Additional details and set up schematics are presented in Karnam *et al.* (2023). Particle image velocimetry was utilised to extract quantitative flow metrics from the C-D plane and the Twinjet plane at both operating conditions. Flow images were acquired using a pair of LaVision Imager Intense CCD cameras, each with a 1376×1040 pixel array (pixel pitch $= 6.45$ µm). The flow field was illuminated by an Evergreen Dual Pulse Nd:YAG laser operating at a peak frequency of 5 Hz at 532 nm (170 mJ per pulse).

A pair of Nikon (NIKKOR) 50 mm lenses at $f/16$ aperture were paired with the cameras to maximise the measurement area. An optical bandpass filter (wavelength, 532 nm; optical density, 6; full-width half-maximum (FWHM), 10 nm) was used with each lens to avoid capturing light from surface/stray reflections without affecting the light reflected off the seed particles. A knife edge was also used to limit the spread of the laser sheet to prevent strong reflections from the nozzle lip bleeding into the image frame. The choice of the lens was made to accommodate both the jets when viewing the Twinjet plane. The interval between successive frames was set to 0.5 µs to minimise measurement lag given the large field of view provided by the lens. The core flow was seeded using alumina sourced from Buehler Inc. with a manufacturer specified size of 0.3 µm. The ambient was seeded using fog from a water-based fog generator with a manufacturer-specified size of 1 µm.

For each test condition a series of 2400 images were recorded for image filtering and vector field computation. Key post-processing parameters are listed in table 2. Two cross-correlation passes were performed with an overlap of 50 % between sampling windows for vector identification and filtering. The readers are referred to Jeun *et al.* (2022) and Karnam *et al.* (2022) for a detailed description of the apparatus and particle lag analysis. The methodology of higher-order metric computation is discussed in Appendix C. The Stokes number that characterises the accuracy of particle tracking analysis was computed to be $St_k \approx 0.11$ which satisfies the commonly accepted criteria of $St_k \ll 1$.

The choice of low-temperature operating conditions employed for this study was guided by two key factors. First, studying flow behaviour at ambient conditions provides valuable insights into highly dynamic flow features such as screech instabilities that are relevant to propulsive nozzle systems and related fields, such as high-pressure injection

Interrogation window – initial (pixel)	128×128
Interrogation window – final (pixel)	16×16
Frame separation (μs)	0.5
Exposure time (ns)	500
Field of view per camera (h)	6.58×4.68
Digital resolution (pixel/h)	208.46
Vector resolution ($l \times w$)	174×130

Table 2. The PIV parameters.

systems. Second, limitations in the fabrication process for the proposed design led to employing 3D-printed nozzles made from ABS (acrylonitrile butadienestyrene) plastic due to challenges associated with manufacturing metallic nozzles thus restricting the study to ambient temperature conditions. It must also be noted that low-temperature operation highlights screeching phenomena in supersonic nozzles, which are diminished at higher operating conditions (Heeb *et al.* 2013). Understanding the behaviour of these jets at lower temperatures serves as a foundation for future investigations at elevated operating temperatures. The selection of operating conditions was further informed by Karnam *et al.* (2023), where rectangular and circular nozzle geometries demonstrated significant instability characteristics at NPR 2.6 and NPR 3. As a result, the present nozzle design was tested within these operating ranges, with the findings discussed in the subsequent sections.

3. Results and discussion

The experimental and numerical results are presented in the following order. An initial discussion on the far field acoustic results obtained from experiments is provided to identify trends in noise propagation. This is followed by an examination of flow features obtained from high-speed schlieren images. Finally, results of flow field measurement from PIV coupled with the spatial and temporal spectral analysis results from schlieren are used to identify the sources of jet instabilities. Due to the wealth of information uncovered in the course of analysis, the current results focus primarily on the Twinjet plane. While an independent and in-depth analysis is being considered for the data obtained from the C-D plane of the jet, some relevant results are discussed in this study to provide a wholistic understanding of jet behaviour.

3.1. *Far-field acoustic results*

Results obtained from the experimental far field acoustics tests are presented for the overexpanded conditions of NPR 2.6 and NPR 3. The Strouhal number ranges were computed using the isentropic exit velocity ($U_{j,\,NPR\,2.6} = 377.7$ m s^{-1}, $U_{j,\,NPR\,3} = 399.9$ m s^{-1}) and the nozzle equivalent diameter ($St = fD_e/U_j$). Figure 2 summarises the acoustic intensity and directivity across two observation planes, the Symmetry plane, and the Twinjet plane as introduced in figure 1(*b,c*). For clarity, the results from the Symmetry plane are denoted with a solid line and those from the Twinjet plane are denoted using a dotted line. Additionally, in the OASPL plot values from the Symmetry plane are represented with hollow symbols and values from Twinjet plane are represented with solid symbols.

Figures 2(*a*) and 2(*b*) reveal the frequency spectra obtained from two azimuthal angles. The spectra are offset by a value of 20dB for clear delineation across NPRs and observation
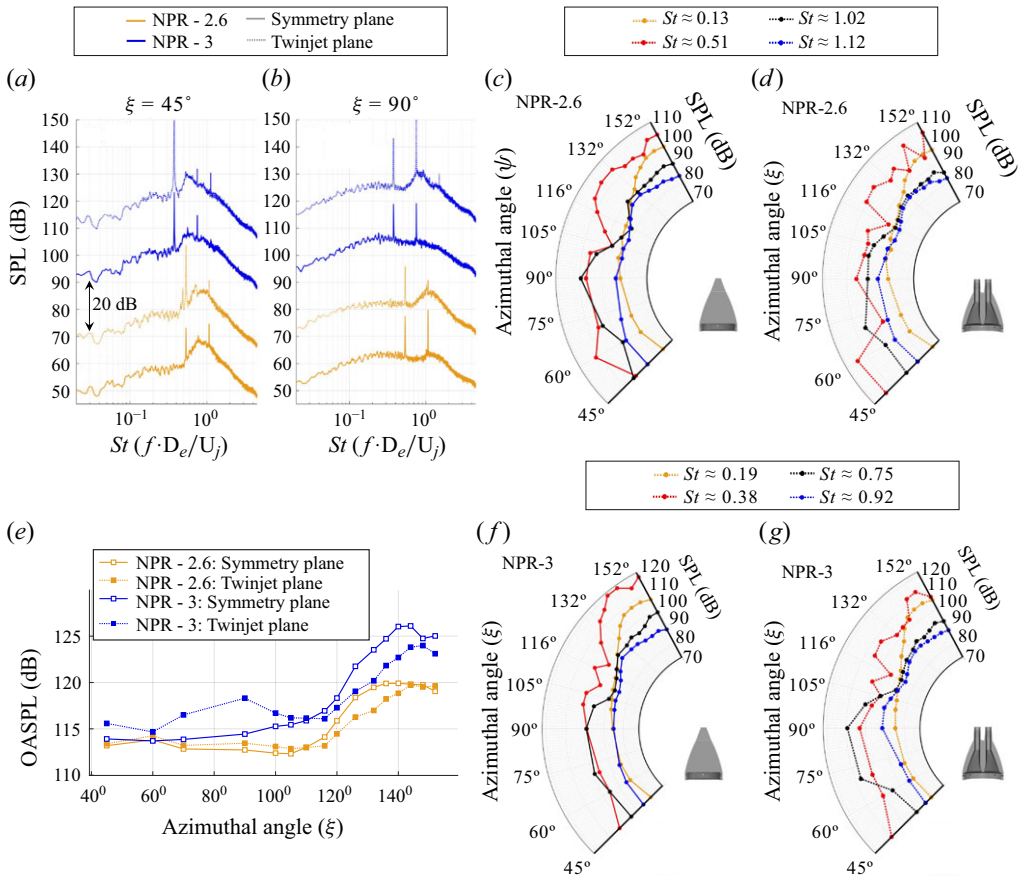
Figure 2. Far field acoustic results for NPR 2.6 (gold) and NPR 3 (blue). Staggered frequency spectra from the Symmetry plane (solid) and Twinjet plane (dotted) from azimuthal angles (*a*) $\xi = 45°$, (*b*) $\xi = 90°$. Frequency specific directivities for NPR 2.6 – (*c*) Symmetry plane, (*d*) Twinjet plane; NPR 3 – (*f*) Symmetry plane, (*g*) Twinjet plane. (*e*) The OASPL distributions from both planes.

planes. At NPR 2.6 (represented in gold), a prominent screech tone was observed at $St \approx 0.51$ (10.4 kHz) with the harmonic identified at $St \approx 1.02$ (20.8 kHz). At the upstream angle of $\xi = 45°$, the SPL values from these frequencies were comparable in the Symmetry plane as shown in figure 2(*a*) while the primary screech tone was dominant in the Twinjet plane.

This trend was partly reproduced at $\xi = 90°$, as seen in figure 2(*b*) accompanied by a significant increase in magnitudes of the primary screech tone (+4.3 dB) and the harmonic (+5.6 dB) when compared with the levels recorded at $\xi = 45°$.

At NPR 3 (represented in blue), the primary screech tone was revealed at $St \approx 0.38$ (8.15 kHz) accompanied by a harmonic at $St \approx 0.75$ (16.25 kHz). The acoustic levels at $\xi = 45°$ were largely dominated by the primary screech on both observation planes as seen in figure 2(*a*). Conversely, in the jet normal direction at $\xi = 90°$, the primary screech tones and first harmonic exhibited comparable SPL levels across both observation planes as seen in figure 2(*b*). Notably, a significant overlap between the broadband shock associated noise (BBSN) frequencies and the first harmonic frequency was observed that resulted in an intensity match with the primary tone in the Twinjet plane. This pattern of harmonic and BBSN frequency concurrence in twin-jet arrangements, previously noted in the research conducted by Jeun *et al.* (2022), Samimy *et al.* (2023) and

Kuo, Cluts & Samimy (2017), underscores a complex interplay between harmonic generation and shock–turbulence interactions that contribute to shock-associated noise production.

To deduce the directivity patterns, four distinct peak frequencies were identified across all directivity angles at each operating condition. These plots are presented as pairs visualising directivity patterns from the Symmetry plane and Twinjet plane in figures 2(*c,d*) and 2(*f,g*) for NPR 2.6 and NPR 3, respectively. The lines correspond to the large scale turbulence (LST) noise peak (gold), the primary screech tone (red), the first harmonic (black) and the BBSN peak (blue) relevant to each condition. At NPR 2.6, the LST frequency recorded at $St \approx 0.13$ (2.8 kHz) exhibited peak noise levels at the far downstream angles ($\xi = 148°$, spectra; Appendix A) in both the Symmetry plane and Twinjet plane as seen in figures 2(*c*) and 2(*d*). This behaviour is well documented (Tam 1995) and expected due to the growth and collapse of large scale turbulent structures that occurs towards the end of the jet potential core (Tam *et al.* 2008). The directivity pattern for the primary screech tone in the Symmetry plane resembles Norum's (Norum 1983) prediction for circular jets. The similarity between Norum's data and the current result could likely be linked to the symmetric exit area of the square nozzles in the current study. In contrast, other non-circular nozzles such as rectangular jets show the emergence of screech tones and the associated harmonics from the shear layers that start from the longer nozzle walls housing the C-D section. The directivity pattern associated with screech tones consist of multiple propagation vectors as documented by Gutmark *et al.* (1990), Gojon *et al.* (2019) and Malla *et al.* (2017). Additionally, findings that associate the production of these screech tones with shock turbulence interaction were deduced from the computational study by Shen & Tam (2002) and from the experimental studies of Panda (1999) and Edgington-Mitchell *et al.* (2021, 2022). The intricate directivity pattern in the Twinjet plane, coupled with that in the Symmetry plane suggests that current nozzle design demonstrates aspects of both symmetric and non-axisymmetric nozzles. The first harmonic exhibited pronounced directivity towards $\xi = 90°$, especially noticeable in the Symmetry plane, whereas diminished noise levels at this frequency were recorded in the Twinjet plane. The BBSN peak frequency was recorded at $St \approx 1.12$ (23 kHz) and showed identical directionality across both planes of observation.

At NPR 3, the LST frequency recorded at $St \approx 0.19$ (4.1 kHz) and the BBSN peak frequency at $St \approx 0.92$ (20 kHz) exhibited patterns consistent with those observed at NPR 2.6. The former frequency peaked towards the downstream angles ($\xi = 144°$, spectrum; Appendix A) and the latter demonstrated peak intensity in the jet normal direction with highest recorded values in the Twinjet plane as seen figures 2(*f*) and 2(*g*). Although the noise distribution of the primary screech tone trended similar to that observed at previous condition within the Symmetry plane, an azimuthal peak was observed at $\xi = 140°$ diverging from the value of $\xi = 126°$ for NPR 2.6. This shift suggests that the generation of large-scale coherent structures could be a prominent feature of the screech production mechanism at NPR 3. Additionally, the first harmonic exhibited a notable increase of ≈ 9.5 dB in the Twinjet plane compared with the Symmetry plane marking a reversal in the trend observed at NPR 2.6. This could be indicative of a significant change in jet behaviour at the higher pressure condition. As documented by Ahn *et al.* (2023) and Karnam *et al.* (2022) it is known that the jets undergo symmetric oscillations in the Twinjet plane at NPR 3. The observed variations in directivity for the screech peak and the harmonic at NPR 2.6, when compared with NPR 3, hint at a distinct mode of jet oscillation contrasting prior findings.

The OASPL presented in figure 2(*e*) encapsulates the cumulative impact across all relevant frequency ranges. For NPR 2.6 the noise levels remain consistent across both

observation planes at the lower azimuthal angles and increase gradually towards the jet downstream. Peak noise levels in the Symmetry plane were recorded at 119.9 dB at the azimuthal angle of $\xi = 140°$, while the noise peak in Twinjet plane was recorded at 119.7 dB at the azimuthal location of $\xi = 144°$. At NPR 3, noise levels from the Twinjet plane clearly dominate the upstream and jet normal directions. This can be attributed to the first harmonic tone from the prior discussion on frequency directivity. However, the noise generated from the Symmetry plane is dominant in the downstream angles primarily due to the symmetric oscillation mode that the jets undergo at this condition. Peak noise levels of 126.1 dB ($\xi = 144°$) and 124 dB ($\xi = 148°$) were recorded in the Symmetry and Twinjet planes, respectively (additional spectra included in Appendix A).

3.2. *Flow field: schlieren image analysis – primary screech frequency*

High-speed schlieren images were analysed to identify spatial and temporal flow variations using spectral analyses. This section examines data acquired at the acquisition rate of 41 kHz (F_1). Temporal decomposition of the image set was performed using the spectral proper orthogonal decomposition (SPOD) technique as detailed by Schmidt & Colonius (2020). This was coupled with an implementation of the spatial decomposition technique outlined by Edgington-Mitchell *et al.* (2021, 2022) at the screech frequency to identify the corresponding bidirectional wave propagation.

An initial assessment of the jet structure was conducted by examining the average and statistical intensity distributions from schlieren images as depicted in figure 3. The logarithmic intensity standard deviation ($\log_{10} \sigma_i$, where σ_i is the intensity standard deviation), computed using the fluctuating component of the light intensity at each spatial location, can be a useful technique to visualise the effect of periodic flow oscillations on the jet near field (Edgington-Mitchell 2019; Karnam *et al.* 2023). At NPR 2.6, a clear shock train emerging from both nozzles was observed as seen in figure 3(*a*). The overexpanded nature of the flow led to the formation of a prominent shock system that extends up to X/*h* ≈ 5.2 from the nozzle exit. In contrast at NPR 3, the flow exits into a weaker oblique shock
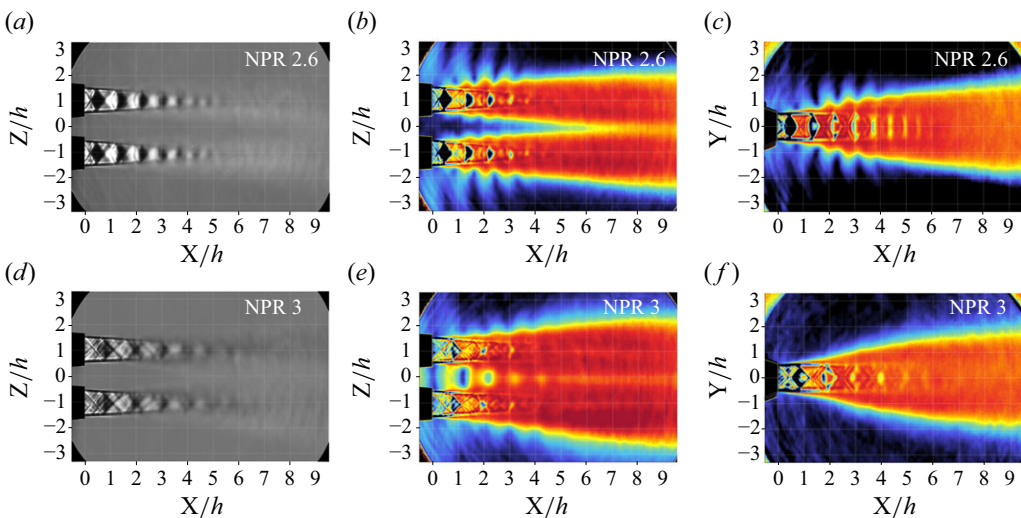

Figure 3. Metrics derived from schlieren images (image intensity normalised with peak values), for NPR 2.6 (*a–c*), NPR 3 (*d–f*). Temporal average schlieren images (*a,d*). Logarithmic intensity standard deviation for Twinjet plane (*b,e*). Logarithmic intensity standard deviation for C-D plane (*c,f*).

system due to the lower degree of overexpansion compared with the previous condition as seen in figure 3(*d*). The secondary shock system that is characteristic of sharp throat nozzles (Munday *et al.* 2011; Karnam *et al.* 2023) and was previously overshadowed by the exit shock system emerges at this condition. The shock train extends from the nozzle exit to X/*h* ≈ 6.3. In comparison with NPR 2.6, the shock-expansion system at NPR 3 are fainter beyond X/*h* = 3 and lack spatial clarity due to the intense flow oscillations that alter the average location of these shocks.

The manifestation of the screech tones observed in the far field acoustics was captured in the standard deviation profiles depicted in the subsequent figures. Studies (Panda 1999; Edgington-Mitchell 2019; Karnam *et al.* 2023) have shown that screeching jets lead to the formation of standing waves in the jet near field resulting from the superposition of downstream travelling hydrodynamic waves along the jet shear layers and upstream travelling acoustic waves emitted by shock–turbulence interactions. At NPR 2.6, the standing wave pattern on each jet features distinct peaks along both shear layers in the Twinjet plane as seen in figure 3(*b*). The outer shear layers exhibited pronounced crests that extended radially outward with an upstream directivity. Furthermore, the jets exhibit mirror symmetry along the Symmetry plane, with notable alignment of crest locations on both shear layers hinting towards the emergence of coupled oscillations within the Twinjet plane. These features were found to extend along the upper and lower shear layers of the jets in the nozzle C-D plane as depicted in figure 3(*c*). This is a clear indication of coupled instability waves travelling along all shear layers of the jet and aligns with the findings noted in Karnam *et al.* (2023) for rectangular jets operating at the same NPR. A peculiar feature is the lack of standing waves along the inner shear layers at NPR 2.6 in the Twinjet plane. This can be indicative of the presence of destructive wave interference leading to diminished wave amplitudes along the inner shear layers.

The LES study of Ahn *et al.* (2023) and experimental work of Karnam *et al.* (2022) have previously documented the phase locked oscillations observed at NPR 3. The effect of this coupling dynamic is shown in figure 3(*e*). The internozzle region at the higher NPR features a prominent standing wave pattern that extends upstream of the nozzle exit. This is accompanied by a wave pattern that emerges along the outer shear layers. Conversely, no identifiable patterns emerged in the C-D plane of observation as illustrated in figure 3(*f*). This is a strong indication of the spatial instabilities being dominant in the Twinjet plane. Edgington-Mitchell *et al.* (2022) and Li *et al.* (2023) demonstrated the use of temporally averaged schlieren images to compute the spatial wavenumber spectra of supersonic jet shock systems, allowing for the identification of wavenumbers linked to the most distinct shock cells ($k = 2\pi/\lambda_S$ where λ_S is shock cell wavelength). A similar approach was implemented in the current study on the temporal average of the schlieren images and the axial velocity snapshots from the PIV data set as discussed in Appendix B. This led to the extraction of the wavenumbers corresponding to the first (k_{S1}) and second (k_{S2}) shock cells. The inverse correlation between the spatial wavelength of the shock cells and the wavenumber led to a lower k values for the same shock cells at the higher NPR with $k_{S1, NPR\ 2.6} = 7.88$, and $k_{S1, NPR\ 3} = 6.309$, respectively.

While the seminal research by Powell (1953*a*,*b*) indicated acoustic feedback as the primary screech closure mechanism, subsequent work by Shen & Tam (2002), Panda (1999), Mancinelli *et al.* (2019, 2021), Edgington-Mitchell *et al.* (2021*a*,*b*, 2022), Edgington-Mitchell *et al.* (2018) and Nogueira *et al.* (2022*a*,*b*) have provided strong evidence that supports screech generation stems from triadic interactions between *KH* instability waves and the quasisteady shock structure of the jet. These interactions have been known to result in the generation of the three primary components: acoustic waves,

shock leakage and the internal G-JM. These have been documented in circular (Shen & Tam 2002; Edgington-Mitchell *et al.* 2022; Nogueira *et al.* 2022), rectangular (Gojon *et al.* 2019; Karnam *et al.* 2023; Li *et al.* 2023) and elliptical (Edgington-Mitchell *et al.* 2022) nozzles. The primary generation mechanism involves the downstream propagating *KH* instabilities interacting with the shock cell tips impinging on the jet shear layers leading to the generation of acoustic waves. In highly unstable jet states resonance in the internal neutral waves at the screech frequency and the interacting shocks can result in the generation of an upstream travelling wave mode that completes the excitation loop by propagating the flow instability towards the nozzle exit along the internal wall of the jet shear layer. Additionally, unstable perturbations in these jets can lead to shock impingement between consecutive vortices resulting in the leakage of internal pressure waves into the ambient. This was identified as the source of shock leakage by Manning & Lele (2000). In a recent study, Nogueira *et al.* (2024) have formulated a model to predict G-JM waves resulting from these triadic interactions. The current study utilises spatial Fourier decomposition to identify the signatures of the various components of the triadic interaction as discussed in Appendix B. Throughout this discussion the interaction between the first shock cell and the *KH* instability waves is referred to as the optimal interaction (k_{KH}–k_{S1}) and the interaction with the second shock cell is referred to as the suboptimal interaction (k_{KH}–k_{S2}).

In the current study, the block size for SPOD was chosen relative to the acquisition frequency ($N_{F1} = 820$, $N_{F2} = 2240$) to achieve a frequency resolution of 50Hz, aligning with the frequency resolution of the acoustic measurements. To mitigate signal discontinuities between blocks, a Hamming window was employed, featuring a 75 % overlap among blocks. The principal instability frequencies and their associated harmonics within the Nyquist cutoff limits ($Nq_{F1} = 20.5$ kHz, $Nq_{F2} = 56$ kHz) were discerned from the SPOD analyses for both operational conditions. Subsequently, spatial analysis was performed on the energy distributions within the complex plane at each frequency, thereby revealing the directional wave propagation and the spatial wave interactions. The energy distribution associated with the primary mode at $St \approx 0.51$ for NPR 2.6 is shown in figure 4(*a*) which clearly indicates that the jets undergo coupled oscillations in the Twinjet plane. The inner shear layers of the jets were found to be out of phase with each other by π radians, a phenomenon that extends to the outer shear layers as well. Critically, this phase misalignment along the inner shear layers leads to destructive interference resulting in minimal energy levels along the symmetry line in the internozzle region. This is in agreement with the observations made in the intensity standard deviation in figure 3(*b*). Due to this interference, peak energy levels are concentrated along the outer shear layers, specifically from X/h = 1.5 to X/h = 4. Also observed was the upstream acoustic emission from the outer shear layer and the downstream travelling coherent structures along the jet shear layers. Contrary to the energy distribution in figure 4(*a*), the phase distribution does not exhibit mirror symmetry around the nozzle's Symmetry plane. This behaviour is consistent with the results observed in twin circular nozzles in the experimental study by Knast *et al.* (2018) and the LES results of Ahn *et al.* (2021*b*).

However, in both cases the nozzles were purely converging circular nozzles with an internozzle spacing of $s/h = 3$ undergoing corotating helical coupling mode. The result of the spatial decomposition from the SPOD mode and the expected interaction wavenumbers are depicted in figure 4(*b*). As is convention, positive wavenumbers represent downstream propagating waves, and negative wavenumbers represent upstream propagating waves. The contour colours represent the energy intensity expressed in logarithmic scale of the spectral energy content.
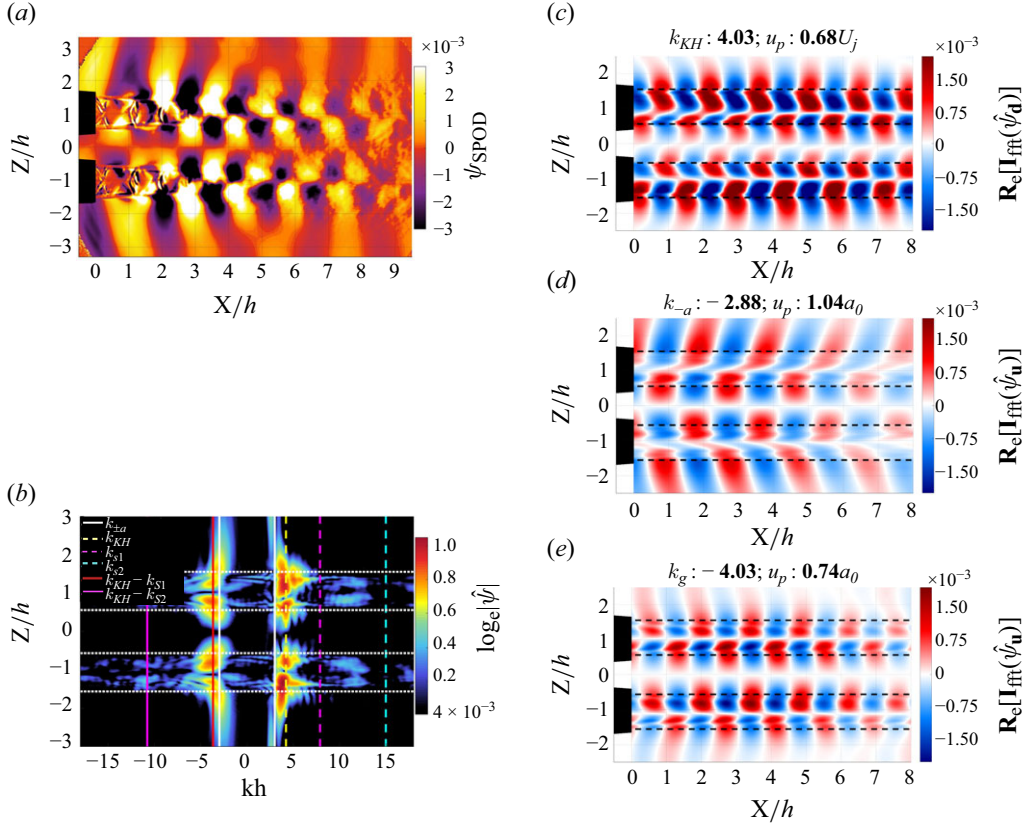
Figure 4. (*a*) Mode-1 SPOD result for NPR 2.6 at $St \approx 0.51$. (*b*) Energy contours for normalised wavenumber (kh) versus radial distance (Z/h). White vertical line, acoustic wavenumber ($k_{\pm a}$); yellow dashed line, *KH* instability wavenumber (k_{KH}); magenta dashed line, first shock wavenumber (k_{S1}); cyan dashed line, second shock wavenumber (k_{S2}); red solid line, optimal interaction ($k_{KH}-k_{S1}$); magenta solid line, suboptimal interaction ($k_{KH}-k_{S2}$); white dotted line, nozzle lip line. (*c*) Reconstructed energy profile for the *KH* instability wave (k_{KH}). (*d*) Reconstructed energy profile for upstream acoustic waves (k_{-a}). (*e*) Reconstructed energy profile for G-JM (k_g). View normal to Twinjet plane.
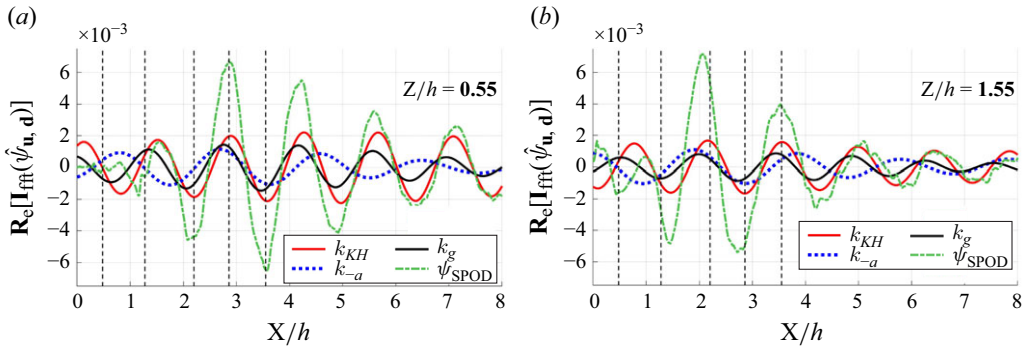

Figure 5. Amplitudes along inner and outer lip line for jet centred at Z/h = 1.05 from SPOD mode ($\psi_{\mathbf{SPOD}}$) and spatial energy profiles: *KH* instability(k_{KH}); acoustic (k_{-a}); G-JM (k_g). Dashed lines are shock cell locations.

While the convective velocity for supersonic flows is widely accepted (Tam & Tanna 1982; Anand *et al.* 2021; Harper-Bourne and Fisher 1973) as being $\approx 0.7U_j$ this value was observed to vary depending on the jet operating condition and nozzle geometry (Saleem *et al.* 2023). Following the methodology of Jeun *et al.* (2022), the wavenumber for the *KH* instability waves was identified by locating the peak energy signature in the downstream direction ($k > 0$). This value is indicated by the yellow dashed line. The red solid line marks the optimal interaction, and the magenta solid line marks the suboptimal interaction. Energy distribution across both the jets was found to be concentrated within the nozzle lip lines indicated by the dashed white lines. The energy peaks were found to be associated with the *KH* instability waves which propagate in the downstream direction. Conversely, notable upstream features appear close to the acoustic speed of sound ($k_{-a} = -2.99$) and represent the acoustic emission generated by the screech tones and the G-JM. The convergence of k_{-a} and the optimal interaction ($k_{KH}-k_{S1} = -3.67$) highlights the influence of the first shock cell in the generation of the primary screech tone. The energy signature associated with the G-JM was identified as the secondary upstream lobe at $k_g = -4.03$. A defining characteristic of G-JM is the presence of high energy concentrations close to the jet shear layer that experience rapid drop off at larger radial locations outside the jet (Edgington-Mitchell *et al.* 2022). This trend was clearly observed at k_g, while the suboptimal interaction ($k_{KH} - k_{S2} = -10.74$) lands in the duct-like region with energy distribution contained entirely within the jet shear layers.

These regions consist of waves with negative phase velocity that can appear at these wavenumbers (Towne *et al.* 2017) that are energised by the suboptimal interaction but have a positive group velocity that prevents them from closing the screech resonance loop. Furthermore, the internozzle region showed minimal energy concentrations across both upstream and downstream domains reinforcing the hypothesis of destructive interference caused due to the phase offset. Figure 4(*c–e*) were generated by reconstructing specific wavenumbers as outlined in Appendix B. This reconstruction allows for the calculation of the phase velocities of the waves which are annotated on each contour. The waveforms associated with the *KH* instability waves are depicted in figure 4(*c*). As observed in the wavenumber spectra, these waves exhibit the highest energy concentrations among all other wave components. The contours illustrate both the phase and likely locations of the coherent structures responsible for generating these waves. Note that the phase offset between the inner and outer shear layer of each individual jet manifests at the nozzle exit and propagates downstream. These waves are characterised by the energy concentrations occurring close to the nozzle lip line permeating the jet hydrodynamic region. The phase disparity between the inner and outer shear layers leads to higher energy levels along the outer shear layers. Notably, the computed phase speed of $0.68U_j$ closely aligns with the initial estimate of $0.7U_j$.

Figure 4(*d*) depicts the energy distribution linked to the acoustic resultant of the triadic interactions directed towards the jet upstream. The waves exhibit a diminishing energy profile moving downstream past $X/h = 3$, suggesting their origination point lies closer to the nozzle exit. It's noteworthy that the phase disparity observed in these acoustic waves aligns with that identified in the SPOD analysis. The contour for the G-JM, depicted in figure 4(*e*), mirrors the phase pattern seen with *KH* instability waves, yet these waves propagate upstream, guided along the shear layers as indicated by the concentrated energy regions close to the lip lines. A distinct difference in energy levels was observed between the inner and outer shear layers. The outer layers experience no significant external interactions apart from shear driven mixing. However, the inner shear layers engage in consistent phase interactions along the axial direction up to $X/h \approx 5$ resulting in increased wave amplitudes. The computed wave speed of $0.74a_0$ for the G-JM coincides with the

observations made in previous studies (Shen & Tam 2002; Edgington-Mitchell *et al.* 2022; Karnam *et al.* 2023) where a_0 is the ambient speed of sound.

A comparison of the wave amplitudes along the inner and outer lip lines from the jet centred on $Z/h = 1.05$ is illustrated in figure 5. The dotted lines mark the locations of the shock inflection points along the jet shear layer and represent the axial span of the first four shock cells. For the inner shear layer, the maximum amplitude identified from the SPOD contour ($\psi_{\textbf{SPOD}}$) was at $X/h = 2.86$, which coincided with the end of the third shock cell as seen in figure 5(*a*). The coincident peaks of $\psi_{\textbf{SPOD}}$ and k_{KH} plots indicate that the coherent structures play a key role in screech generation. Additionally, the energy profiles for both levels gradually increase downstream, reflecting the growth of coherent structures. In contrast, the peak amplitude from the SPOD mode along the outer shear layer was identified at $X/h = 2.06$, ahead of the third shock cell accompanied by a rapid drop in SPOD energy levels as seen in figure 5(*b*).

This behaviour is driven by mixing between the ambient air and the outer shear layers. This trend is partially mimicked by the acoustic component that is generated through the interaction between *KH* instabilities and shock cells. However, the inner shear layers exhibit a more gradual decrease in energy levels due to the coupled interactions spanning the length of the jet. The surge in flow energy and the positioning of the peaks along the outer shear layer highlight the influence of the first shock cell in energising the flow leading to the generation of acoustic and flow instabilities. On the other hand, the amplitudes of the G-JM were more substantial along the inner shear layers driven by jet coupling. It is important to note that true levels for k_g are found in regions inwards of the lip line.

Spatial spectral decomposition was conducted on the dataset for the condition of NPR 3 with the corresponding results depicted in figure 6. Contrary to NPR 2.6, the inner shear layers at NPR 3 show pronounced phase locking with consistent phase match extending the length of the observable field of view as seen in SPOD results illustrated in figure 6(*a*). The outer shear layers, while being phase matched with each other, were found to be π radians out of phase with respect to the inner shear layers. This phenomenon was attributed to the symmetric oscillations in the Twinjet plane (Ahn *et al.* 2021*b*; Karnam *et al.*, 2022; Ahn *et al.* 2023). Additionally, a standing wave was observed in the internozzle region resulting from the superposition of the incident and reflected acoustic waves. The result of the spatial decomposition from the SPOD mode and the expected interaction wavenumbers are depicted in figure 6(*b*). The phase locked behaviour observed in the SPOD mode translated to energy distributions spanning the inner shear layers along both flow directions. Notably, the energy distribution tied to the *KH* instability waves (yellow dashed line) spans across the inner shear layers while also extending across the jets to the outer shear layers. Similarly, distributions associated with the upstream wavenumbers, acoustic emission (white solid lines) and the G-JM ($k = -4.03$), revealed continuous energy bands spanning across the inner shear layers. The optimal interaction (red line) emerges as the key driver behind the generation of the acoustic component and G-JM.

The position of the optimal interaction line indicates that apart from the acoustic component, shock leakage could be an expected resultant. Figure 6(*c–e*) illustrate the reconstructed energy profiles at the k_{kH}, k_{-a} and k_g wavenumbers. For the KH (k_{KH}) instability waves, adjacent shear layers initially display a phase difference smaller than π radians contrasting the behaviour observed for NPR 2.6. As the waves propagate downstream, the phase offset converges towards π radians. Additionally, the region between the jets exhibited higher energy concentration for NPR 3 as seen in figure 6(*c*) that can be attributed to the constructive interference due to the synchronised oscillation of the jets. The computed wave propagation speed of $0.74U_j$ closely aligns with the value of $0.71U_j$ observed from the LES results (Ahn *et al.* 2023). On the other hand, the acoustic
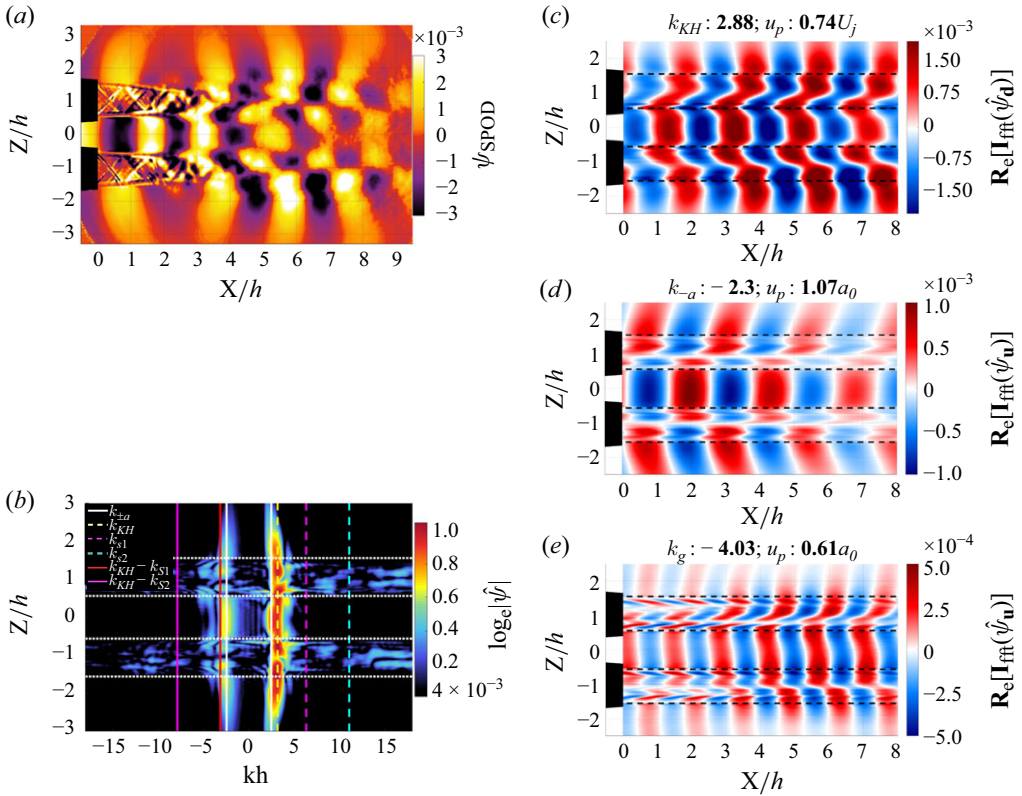
Figure 6. (*a*) Mode-1 SPOD result for NPR 3 at $St \approx 0.38$. (*b*) Energy contours for normalised wavenumber (**kh**) versus radial distance (**Z/h**). White vertical line, acoustic wavenumber ($k_{\pm a}$); yellow dashed line, *KH* instability wavenumber (k_{KH}); magenta dashed line, first shock wavenumber (k_{S1}); cyan dashed line. second shock wavenumber (k_{S2}); red solid line, optimal interaction ($k_{KH}-k_{S1}$); magenta solid line, suboptimal interaction ($k_{KH}-k_{S2}$); white dotted line, nozzle lip line. (*c*) reconstructed energy profile for the *KH* instability wave (k_{KH}). (*d,c*) Reconstructed energy profile for upstream acoustic waves (k_{-a}).(*e*) Reconstructed energy profile for G-JM (k_g). View normal to Twinjet plane.

component is characterised by a constant phase offset of π radians across adjacent shear layers while preserving phase coherence across the inner shear layers as seen in figure 6(*d*). A closer examination revealed the relative dominance of the two components (k_{KH}, k_{-a}) in the SPOD energy contour.

Closer to the nozzle exit the acoustic component's influence is prominent marked by a constant phase difference across adjacent shear layers. Farther downstream at X/h > 4 the influence of the *KH* instability is more pronounced. This is corroborated by the energy profiles of the acoustic component with peak values closer to the nozzle exit. Along the outer shear layer, the influence of *KH* waves is stronger at downstream locations, while upstream acoustics influence regions closer to the nozzle exit. The G-JM is identifiable by the characteristic energy concentrations found close to the nozzle lip line in figure 6(*b*) at $k_g = -4.02$. Figure 6(*e*) depicts the reconstructed energy profiles for k_g. Mirroring the phase coherence followed by the other components, the G-JM originates as a resultant from the optimal interaction with coupled energy magnitudes increasing in amplitude towards the jet downstream. This trend indicates mode amplification driven by shear layer mixing. Characteristically, the energy profiles along the outer shear layers dissipate rapidly at outward radial locations.
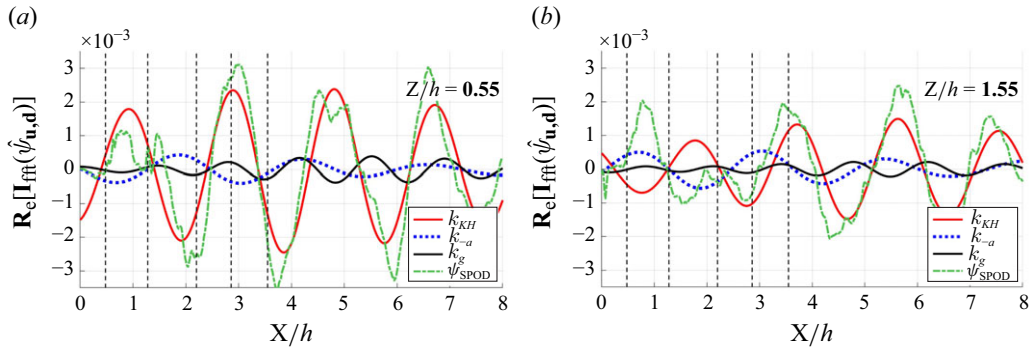
Figure 7. Wave amplitude along inner and outer lip line of the top jet from SPOD mode ($\psi_{\textbf{SPOD}}$) and spatial energy profiles: *KH* instability(k_{KH}); acoustic (k_{-a}); G-JM (k_g). Dashed lines represent shock cell locations.

The wave amplitude comparison extracted along the nozzle lip lines is depicted in figure 7. Along the inner lip line, the flow energy dynamics is predominantly driven by *KH* instabilities as evidenced by the correlation between k_{KH} and $\psi_{\textbf{SPOD}}$ in figure 7(*a*). Peak amplitudes were identified between the third and fourth shock cell and at downstream location of $X/h = 6.5$. The persistent trend of high energy across the jet length illustrates the role played by the first shock cell on the triadic interactions. Conversely the acoustic component is the dominant contributor along the outer shear layer, particularly near the nozzle exit as depicted in figure 7(*b*). The amplitude trends of $\psi_{\textbf{SPOD}}$ align closely with k_{-a} along the first three shock cells, beyond which a shift to k_{KH} was observed. The overall peak amplitude along the outer shear layer occurs at $X/h = 5.8$ for $\psi_{\textbf{SPOD}}$ due phase inversion in relation to the inner shear layer. The trends in k_g amplitudes across both shear layer highlight jet coupling with higher values appearing along the inner shear layer. Across both shear layers the amplitudes of k_g broadly follow the trends exhibited by *KH* instabilities peaking at axial locations similar to k_{KH}. Higher G-JM amplitude along the inner shear layers can be attributed to the onset of mixing in the internozzle region. The energy trends along the inner and outer shear layers for NPR 3 oppose the results discussed for NPR 2.6 (figure 4) where energy concentrations were dominant along the outer shear layers. This emphasises the role of oscillation phase on jet development along inner shear layers where in phase oscillations drives stronger flow fluctuations.

3.3. *Flow field: schlieren image analysis – screech harmonic frequency*

To capture the flow dynamics at higher frequencies at the condition of NPR 2.6 the image acquisition rate was increased to 112 kHz (F_2) thereby extending the Nyquist limit to 56 kHz. This led to a reduction in the field of view to 6 h × 2 h (length × width). A total of 4000 samples were collected at F_2 and an SPOD analysis was performed with a block size of $N_{F2} = 2240$ samples per block with a 75 % overlap between blocks resulting in a frequency resolution of 50 Hz. The findings at the harmonic frequency of $St \approx 1.02$ (20.8 kHz) are illustrated in figure 8. The energy distribution contour from the leading mode of the SPOD results at the harmonic frequency is illustrated in figure 8(*a*). Unlike the primary frequency tone, the inner shear layers displayed symmetric phase-energy distribution at the harmonic frequency. Significant interactions were observed in the internozzle region between $X/h = 1$ and $X/h = 4$ prior to shear layer mixing. The spatial decomposition of the dominant SPOD mode illustrated in figure 8(*b*) unveiled several noteworthy findings. The energy associated with the *KH* instabilities was highly localised
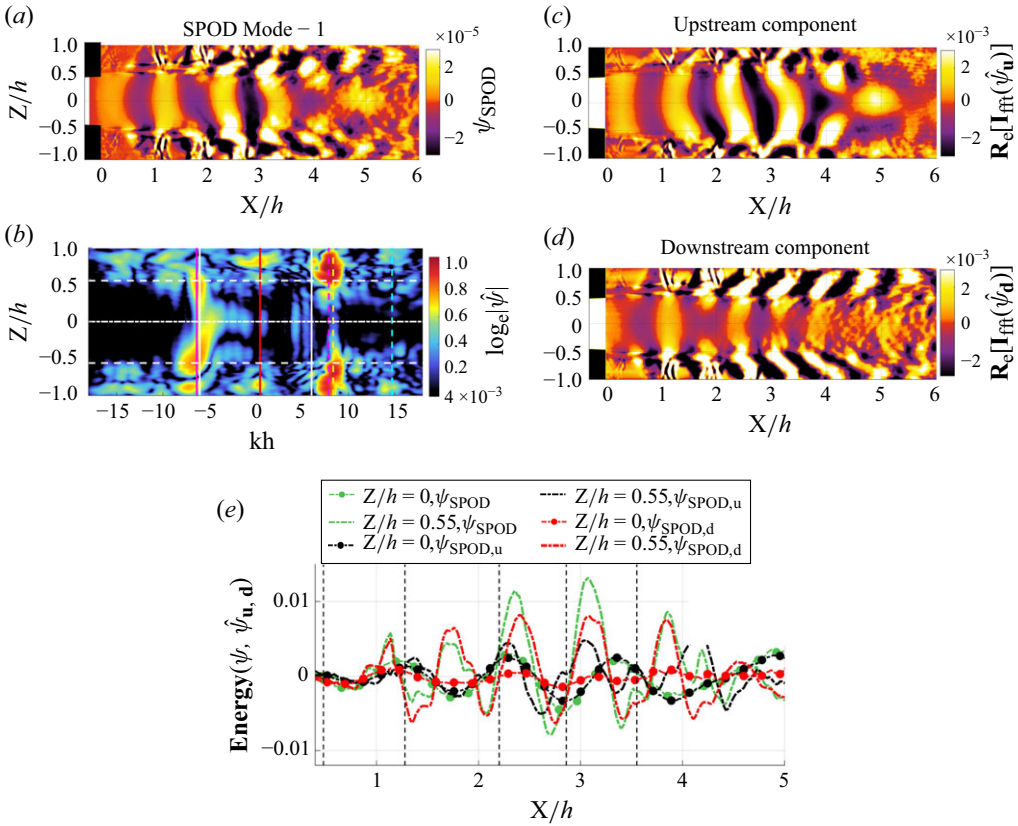
1009 A13-16

Figure 8. Spatial energy distribution for NPR 2.6 at $St \approx 1.02$. (*a*) Energy distribution at mode 1 from SPOD results. (*b*) Contour of energy distribution for normalised wavenumber (**kh**) versus radial distance (**Z/h**). Line nomenclature see figure 7. (*c*) Isolated upstream components. (*d*) Isolated downstream components. (*e*) Energy levels obtained at centreline (Z/h = 0, -•-) and lip line (Z/h = 0.55, ·-·-) from (*b*),(*d*) and (*e*). Vertical dashed lined indicate locations of shock inflection points. View normal to Twinjet plane.

in regions close to the shear layer of the jet at $k_{kH} = 8.1$ with a computed wave propagation speed $u_p = 0.6U_j$. Limited hydrodynamic interactions spanning the internozzle region were also observed in the upstream region of the spatial spectral contour.

The energy signature associated with the upstream acoustic waves ($k_{-a} = -6.03$) was found to be higher on the jet centred at Z/h = −1.55. Examination of the cyclic phase patterns of the SPOD revealed a staggered upstream wave propagation to be the cause of the non-uniform energy distribution. Critically, the triadic interaction between the second shock cell and the *KH* instability waves was identified as a key factor in harmonic production indicated by the position of the interaction wavenumber (magenta line). The distribution in the adjoining wavenumbers resembles the duct-like regions with energy levels fully contained within the jet shear layers. This indicates the absence of the G-JM with the primary closure mechanism being acoustic propagation. These observations are in partial agreement with the computational study of Martin *et al.* (2023) where instability generation of the second harmonic tone in an AR 4 rectangular jet was associated with triadic interactions of *KH* instability waves and shock cells.

However, in the study by Martin *et al.* (2023) a G-JM signature was identified as the closure mechanism for harmonic generation. But unlike the current case, the rectangular

jet in their study exhibited an antisymmetric phase pattern at the harmonic frequency. In the current study, the symmetric oscillations at the harmonic frequency in twinjet configurations can lead to strong wave superposition. This can be a potential factor in altering the energy dynamics from the triadic distribution in favour of the acoustic waves making them the primary method of screech closure. The upstream and downstream flow components from the SPOD mode energy contour were isolated and are illustrated in figure 8(*c,d*). The staggered production of upstream component is clear from figure 8(*c*). Peak energy levels occur close to $X/h = 3.35$ and are driven towards the nozzle exit by continuous production of upstream waves along the shock tips. The non-uniformity in these features can be attributed to the presence of flow, hydrodynamic and acoustic components with the main contribution coming from the hydrodynamic part.

In the regions closer to the nozzle exit, the relative dominance of the acoustic component leads to a uniform phase distribution. On the other hand, the downstream propagating flow structures feature strong energy concentrations in regions close to the nozzle lip line. These areas are typically dominated by coherent flow structures seen in figure 8(*d*). Axial energy variations from these contours were extracted along the nozzle symmetry line ($Z/h = 0$) and the inner lip line ($Z/h = 0.55$) and are depicted in figure 8(*e*). Black plots indicate upstream component, red plots indicate the downstream component, and green plots indicate the overall SPOD mode energy. Values from the centreline are denoted by -•-, while those from the lip line are denoted by ··-. The overall peak was identified in the SPOD mode energy along the nozzle lip line $X/h = 3.05$ depicted by the dashed green line. Notably, the intensity levels for the SPOD mode energy and the upstream components (black, -•-) were identical along the nozzle centreline indicating the dominance of acoustics in the internozzle region. Peak energy levels for the downstream components (red, ··-) were identified along the nozzle lip line as expected due to the coherent structures traversing along the shear layers. This contributed to the SPOD mode energy in the shear layer mimicking the behaviour of the pure downstream components. The locations of the peak energy levels after the second shock cell reinforce the prior discussion attributing the suboptimal interaction as the primary driver for harmonic instability generation.

The temporal and spatial energy distributions for the condition of NPR 3 at $St \approx 0.75$ are illustrated in figure 9. Figures 6 and 9 originate from the same dataset and share the larger field of view. The SPOD mode energy results depicted in figure 9(*a*) show identical symmetric phase energy distribution as observed in the first harmonic results for NPR 2.6. Shear layer phase locking observed at the primary screech frequency of $St \approx 0.38$ is also evident in the first harmonic at NPR 3. Moreover, a phase deviation was noted in the outer shear layers relative to the inner ones, along with a noticeable disparity in energy levels between the inner and outer shear layers. The higher mixing experienced by the outer shear layers resulted in rapid reduction in energy levels along the axial direction. In contrast, the inner shear layers show an increase in overall energy along the axial direction peaking close to $X/h = 4$. Beyond this location the effect of flow mixing leads to rapid deterioration of the shear layer boundary definition. The spatial decomposition results illustrated in figure 9(*b*) show trends similar to those observed at NPR 2.6. Utilising the *KH* instability wavenumber at $k_{KH} = 6.23$ the phase velocity of the coherent structures in the downstream direction was computed to be $0.68U_j$ which is lower than the computed phase velocity at the primary screech frequency. Additionally, the triadic interaction between the *KH* instability wave and the second shock, $k_{KH} - k_{S2}$, was identified to strongly influence the generation of the instability tone. This observation is critical as it emphasises the effect of optimal and suboptimal interaction on the flow.
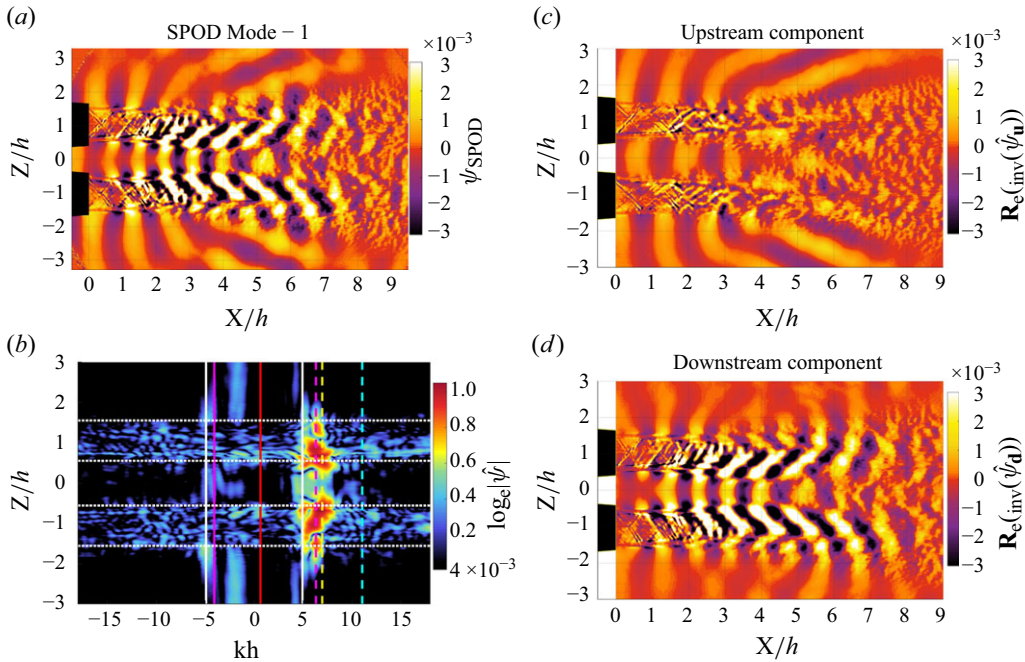
Figure 9. Spatial energy distribution for NPR 3 at $St \approx 0.75$. (*a*) Energy distribution at mode 1 from SPOD results. (*b*) Contour of energy distribution for normalised wavenumber (**kh**) versus radial distance (**Z/h**). Line nomenclature see figure 7(*c*). (*c*) Isolated upstream components. (*d*) Isolated downstream components. View normal to twinjet plane.

Although the precise nature of the interaction that leads to the symmetric or antisymmetric phase behaviour is not fully understood, it is apparent that the suboptimal interaction consistently leads to phase symmetry across the inner shear layers. An interesting note was the absence of energy signatures associated with G-JM indicating that screech closure was once again driven primarily by the upstream propagation of the acoustic component. Isolated upstream and downstream SPOD contours are illustrated in figures 9(*c*) and 9(*d*), respectively. The majority of energy from flow structures was found to be concentrated in the coherent structures along the inner shear layers, primarily within the downstream flow component. Conversely, the acoustic component dominated the space between the nozzles and along the outer shear layers. A notable observation from the flow separation analysis was the detection of oblique waves, which originate from the outer shear layers of the jet and propagate upstream as seen in figure 9(*c*).

This phenomenon aligns with findings from the SPOD analysis of the LES data as reported in Ahn *et al.* (2023). These oblique waves were found to originate near $X/h = 6$, exhibiting an angular directivity of 58° relative to the jet centreline (with the nozzle exit located at 0°). Considering the angular placement of far-field microphones, these waves are the likely cause of the SPL spikes observed in the 90° and 100° microphones shown in figure 2(*g*) at this frequency. In the following section results from PIV analysis will be discussed to understand the effect of the flow instabilities on critical flow metrics.

3.4. *Flow field: PIV*

Results were extracted from PIV images using a three strep postprocessing technique. This consisted of the cross-correlation computations, followed by a correlation accuracy check
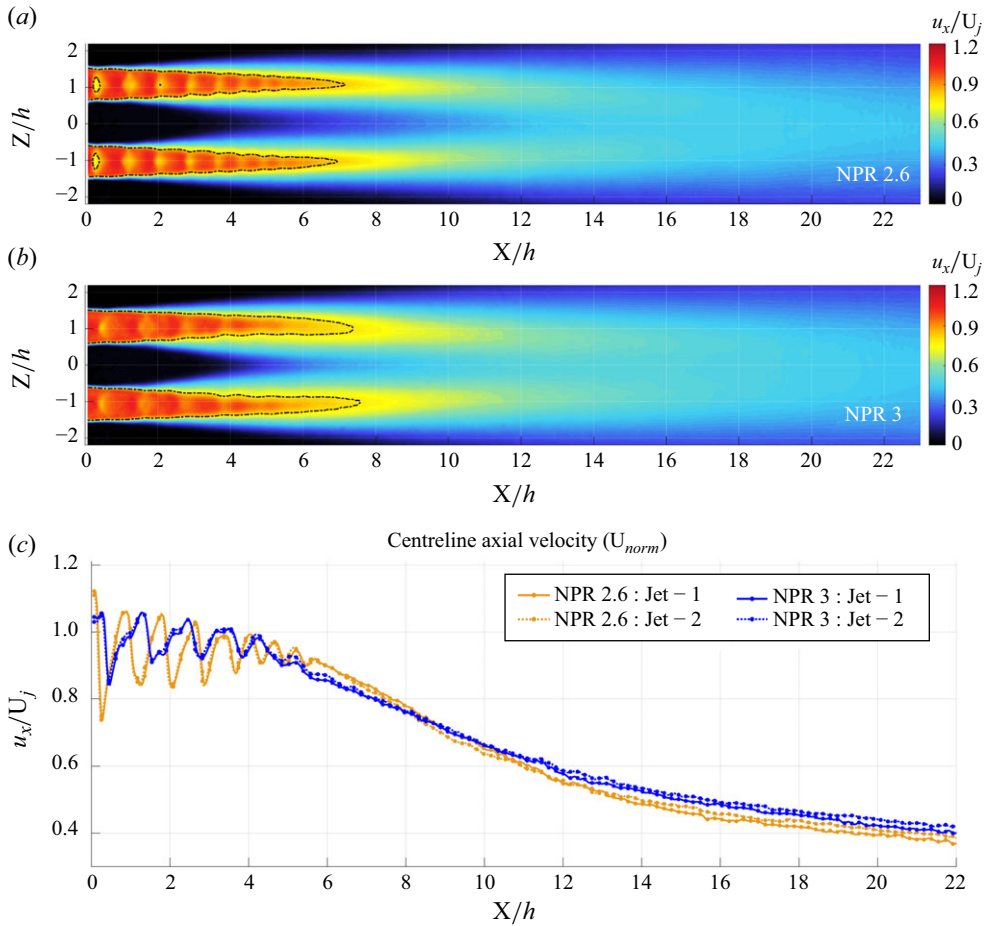
Figure 10. Axial velocity contours: (*a*) NPR 2.6; (*b*) NPR 3. (*c*) Axial velocity values along geometric centreines for NPR 2.6 and NPR 3. Black dashed line represents the sonic line ($M_{local} = 1$). View normal to Twinjet plane.

using vector peak ratio (Q), where vector groups with $Q < 1.5$ were discarded, as values approaching 1 could indicate random correlation peaks unrelated to particle locations (LaVison GmbH 2017). Finally, a local dynamic median filter was used to identify large erroneous vectors based on an root-mean-square–median difference criteria applied across both axial and radial vector components simultaneously. This filtering stage was repeated over two iterations to identify and recompute outliers with a local mean value. The final vector field consisted of 174×130 (length $\times$ width) vectors per camera resulting in a vector density of one vector every 0.63 mm. A traversable twin camera set-up was utilised to capture images resulting in a total field of view of $23.4h \times 4.68h$ (accounting for image overlap and stitching) in the axial and radial directions, respectively.

The average normalised axial velocity profiles for the conditions of NPR 2.6 and NPR 3 are illustrated in figure 10. The formulation proposed by André, Castelain & Bailly (2014) was implemented to compute local Mach number from the mean velocity using

$$M = \left\{ \frac{u^2_{mean}}{\gamma R T_t - u^2_{mean}(\gamma - 1)/2} \right\}^{1/2}, \quad (3.1)$$

where M is the local Mach number, u_{mean} is the mean velocity of the flow ($u_{mean} = (u_x^2 + u_y^2)^{0.5}$) and T_t is the total temperature of the plenum. Since the nozzle operates at ambient temperature, it can be assumed that the variation in the jet total temperature and the reservoir temperature are negligible. The sonic line ($M_{local} = 1$) was extracted from the local Mach number contours and is overlaid as a black dashed line in figure 10.

At NPR 2.6, the experimental results showed the formation of a Mach disc close to the nozzle exit X/h = 0.21 in both the jets as seen in figure 10(*a*). The termination of the supersonic core was identified at X/h = 6.9 from the nozzle exit marked by the sonic line. A constant reduction in the radial span of the jet supersonic regions was noted with the side closer to the symmetry line undergoing accelerated degradation compared with the side along the outer shear layers. Interactions between the jets along the symmetry line were minimal up to X/h = 3.6 beyond which a notable increase in axial velocity was observed. This axial position coincides with the strong antisymmetric coupling observed in the SPOD profiles in figure 4(*a*). and the minimal energy zone in the internozzle region from the intensity standard deviation in figure 3(*b*). Peak mixing velocity in the internozzle region was observed close to X/h = 15 beyond which the inner shear layers merged and were indistinguishable from each other. Subsequently, the jets coalesce and continue as a single jet in the observable domain accompanied by a steady inward deflection of the outer shear layers towards the nozzle symmetry line. For NPR 3, the supersonic jet core extends up to X/h = 7.4 from the nozzle exit, driven by the higher jet operating condition as seen in figure 10(*b*). No Mach disk formation was observed at this condition. Though pronounced oscillations induced by screech were observed at NPR 3, they did not alter the onset of mixing along the inner shear layers which started at X/h = 3.7, similar to NPR 2.6.

However, the rapid increase in the axial velocity along the nozzle symmetry plane indicated that the jets undergo more intense mixing at NPR 3. The degradation of the jet core along the inner shear layers was immediately apparent past X/h = 2.8 marked by the rapid thickening of the inner shear layers. This resulted in the jets demonstrating a strong deflection towards the symmetry line. The enhanced mixing along the symmetry line culminated in the complete merging of the inner shear layers by X/h = 14, beyond which the jets coalesce into a single column. The centreline axial velocities are presented in figure 10(*c*) and highlight the axial locations of the shock-expansion pairs for both operating conditions. The length of the potential core, typically defined as the axial location where the local axial velocity drops below 95 % of U_j, was located at X/h = 5.2 for NPR 2.6 and at X/h = 4.47 for NPR 3. Notably, the centreline velocities for all cases converge once shear layer merging begins at X/h = 15.

A clearer understanding of the flow dynamics can be achieved by analysing the turbulence intensities and Reynold's stresses that highlight the isotropic and anisotropic turbulence features. Figures 11 and 12 illustrate these quantities as measured for NPR 2.6 and NPR 3, respectively. Also highlighted are the locations of the shock inflection points on the jet shear layers to help quantify the spatial span of the shock cells. At NPR 2.6, seven prominent shock cells were identified as seen in figure 11(*a*). The imperfect nature of flow expansion leads to constant reduction in the axial shock cell width driven by the pressure equalisation between the supersonic core and the ambient air.

The average shock cell width across the first three shocks was computed as 0.844h. The turbulence kinetic energy (TKE) distribution in figure 11(*b*) illustrates the distribution of isotropic turbulence intensity with clear peaks emerging in the outer shear layers of the jets and comparatively low levels along the nozzle symmetry line. This reduction is the consequence of the antisymmetric phase coupling observed in the inner shear layers in schlieren image analysis results discussed in § 3.2, figure 4(*c*). Additionally, the coupled nature of interactions occurring along the inner shear layers led to faster

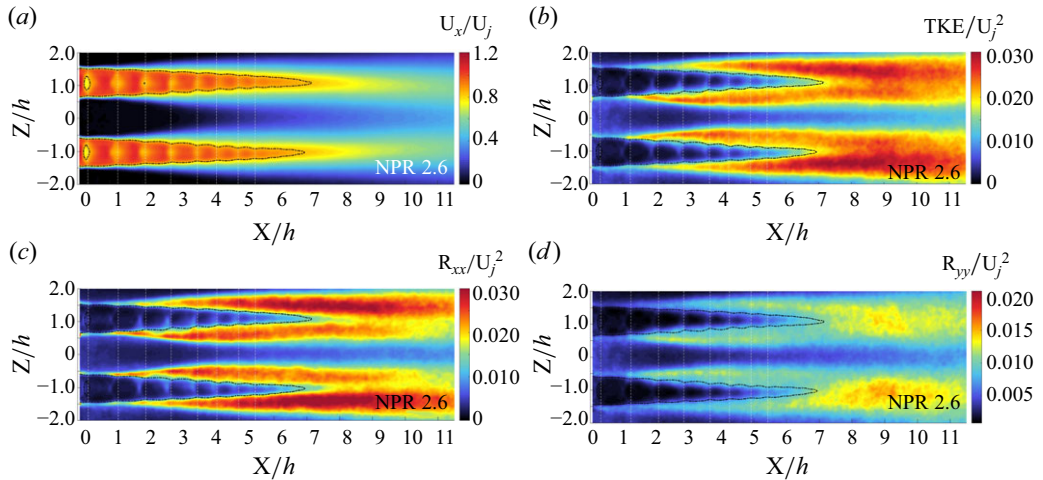Figure 11. Average axial velocity and turbulence quantities for NPR 2.6. (*a*) Normalised axial velocity. (*b*) Normalised TKE. (*c*) Normalised axial reynolds stresses (R_{xx}). (*d*) Normalised radial reynolds stresses (R_{yy}). Black dashed line indicates the sonic line. White dashed lined indicate the location of the shock inflection points.

shear layer spreading as noted by the uneven growth across the inner and outer shear layers. The Reynolds stress profiles presented in figures 11(*c*) and 11(*d*) highlight the influence of the axial and radial velocity components on turbulence development. The axial stresses tend to be dominant driven by the larger fluctuation levels that occur along the streamwise direction. The readers must note that the intensity scale for the R_{yy} distributions has been modified to better reveal flow structures. The axial stresses (R_{xx}) primarily influence turbulence production along the shear layers as indicated by the peak distributions observed in figure 11(*c*).

A notable increase in R_{xx} that indicates the onset of shear layer expansion was identified at $X/h = 1.24$, just aft of the first shock cell. This observation aligns with the findings from § 3.2 which emphasises the influence of triadic interactions between turbulent structures and the first shock cell being a critical component of instability closure. In comparison, the stress levels along the outer shear layers reach matching levels at $X/h = 2.16$, just aft of the second shock cell, close to the peak energy location observed in the SPOD profile in figure 5(*b*). While the radial stresses exhibit comparable patterns along the shear layers, their peak values were identified more internally relative to the shear layer boundaries. This can be attributed to radial fluctuations in flow velocity as illustrated in figure 11(*d*). A notable finding is the minimal turbulence levels within the supersonic core of the jets across all energy distributions. This is anticipated considering that the jet oscillations at NPR 2.6 lack the amplitude to notably disturb the shock train, which would induce rapid velocity changes.

For NPR 3, the turbulence and shear stress profiles from the experimental data are illustrated in figure 12. While the distribution of peak turbulence levels along the outer shear layers broadly resembles that of NPR 2.6, distinct differences are evident. The TKE distribution revealed a large increase in radial jet spreading driven by the symmetric phase locked oscillations of the inner shear layers in the Twinjet plane shown in figure 12(*b*). A prominent feature observed across TKE, R_{xx} and R_{yy} profiles was the distinct branching of flow energy along the inner shear layers and into the internozzle regions originating from $X/h = 1.1$ and reaching maximum radial span at $X/h = 5.2$, beyond the fourth shock
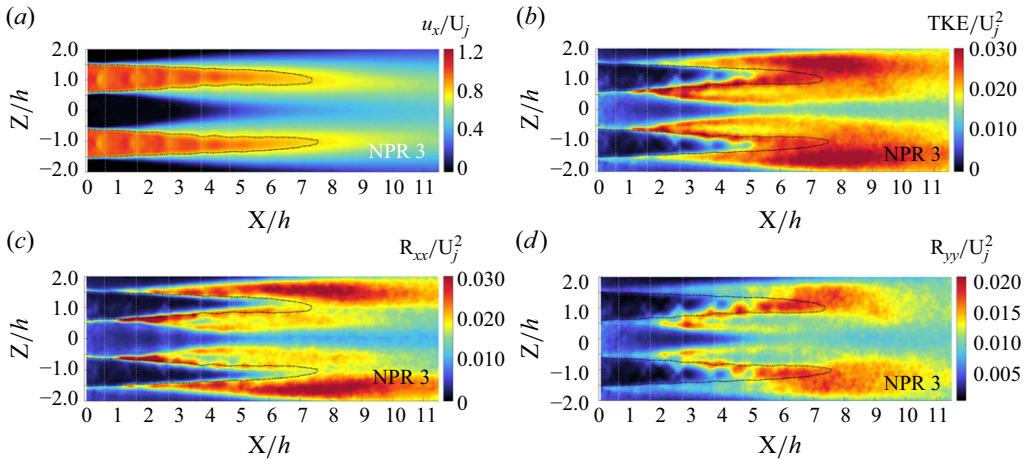
Figure 12. Average axial velocity and turbulence quantities for NPR 3. (*a*) Normalised axial velocity. (*b*) Normalised TKE. (*c*) Normalised axial reynolds stresses (R_{xx}). (*d*) Normalised radial reynolds stresses (R_{yy}). Black dashed line indicates the sonic line. White dashed lined indicate the location of the shock inflection points.

cell. Turbulence peaks were identified aft of the first shock cell at $X/h = 2.2$ along the inner shear layer mirroring the findings from the SPOD analysis discussed in § 3.2. Notably, elevated TKE levels were observed in the trailing region of the supersonic core from $X/h \approx 5$ to $X/h = 7.4$ deviating from the trend observed for NPR 2.6. A closer examination of the R_{xx} and R_{yy} revealed some interesting findings. In figure 12(*c*), axial velocity fluctuations led to high shear stress concentrations along the inner shear layer spanning the first three shock cells between $X/h = 1.1$ and $X/h = 4$. Beyond this region the rapid onset of mixing led to dissipation of the shear stresses. On the other hand, the axial stresses along the outer shear layers showed gradual growth in the streamwise direction with peak values observed close to $X/h = 7.5$. These fluctuations were notably absent in regions inside the supersonic core. In contrast, shear stress peaks of R_{yy} driven by strong radial velocity fluctuations were identified inside the trailing edge of the supersonic core in the same axial range stated above as seen in figure 12(*d*). This suggests that the amplitude of flow oscillation plays a vital role in shaping the core turbulence distribution in highly screeching jets. Moreover, the symmetric coupling observed in twin jet set-ups can greatly influence the amplitudes of jet oscillations, as evidenced by the comparative results for NPR 2.6 and NPR 3.

3.5. *Flow field: proper-orthogonal-decomposition-based selective reconstruction*

To assess the impact of the jet oscillation amplitude on instability tone generation, a reconstruction study was implemented based on the snapshot method of proper orthogonal decomposition (POD) formulated by Sirovich (1987). Research by Oberleithner *et al.* (2011) and Edgington-Mitchell *et al.* (2014) has demonstrated that in flows with periodic instability generation, the first two POD modes fully capture the complete oscillation cycle in flows dominated by periodic instabilities. Additionally, the temporal coefficients associated with these modes are coupled with each other and produce a circular pattern when plotted in a correlated phase space.

This relationship allows for these modes to be utilised in flow reconstruction and identification of the dominant flow features. The current analysis employed the
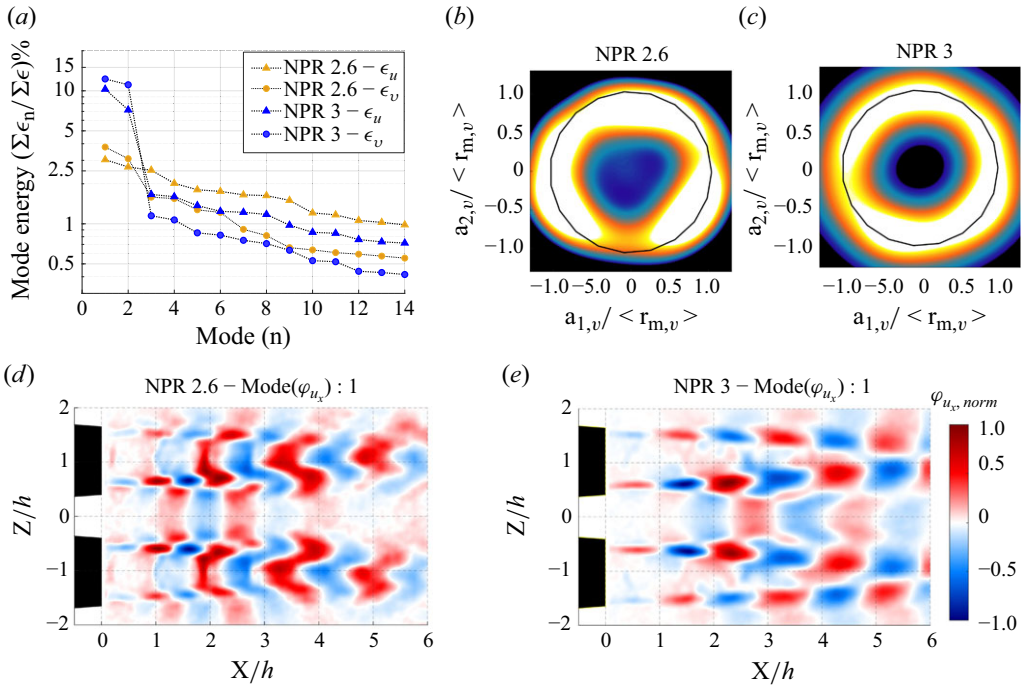
Figure 13. The POD mode energies and phase portraits. (*a*) Energy percentage of individual mode energies (ϵ) from experiment. Here ▲, axial velocity(*u*) components; ●, radial velocity(*v*) components; NPR 2.6, gold; NPR 3, blue. Phase portrait of first two normalised POD temporal components extracted from radial velocity snapshots for (*b*) NPR 2.6 and (*c*) NPR 3. First axial velocity POD mode (φ_{u_x}) for (*d*) NPR 2.6 and (*e*) NPR 3. The phase portraits are normalised using the $r_m = \sqrt{a_1^2 + a_2^2}$ where a_1 and a_2 are the temporal coefficient for the respective POD mode.

methodology from Oberleithner *et al.* (2011) to compute the POD modes from the axial and radial velocity components. The energy distribution of the POD modes and the phase portraits computed from the radial velocity (*v*) components are presented in figure 13. Energy trends from the first fifteen modes are illustrated in figure 13(*a*). The plot depicts mode energy distribution from axial (*u*) and radial velocities with increasing mode value.

The distribution of energy across the first two modes at NPR 2.6 and NPR 3 revealed significant insights into the dynamics of jet oscillations. At NPR 2.6, the first two axial modes accounted for 5.7 % of the total energy, while the radial modes contributed to 6.87 %. In contrast, at NPR 3, the energy contribution from the first two modes increased significantly to 17.5 % for axial modes and 23.4 % for radial modes. This increase in energy levels at NPR 3 is anticipated, considering the phase-locked oscillations that disturb the jets, resulting in substantial flow fluctuations compared with NPR 2.6. Notably, the energy proportion of the first two radial modes exceeds that of the axial modes. Despite axial velocity components typically harbouring more absolute energy than radial components, the jets undergo higher relative amplitude fluctuations in the radial direction, thus yielding a higher relative energy in these modes. The result of these rapid radial oscillations was the large concentrations of radial Reynold's stresses observed in the interior regions of the jets. The temporal components associated with the first two radial POD modes were utilised to construct phase portraits as illustrated in figure 13(*b*,*c*). These contours represented as a probability density function distribution exhibited a pronounced circular

pattern across both operating conditions. This pattern indicates that the first two modes are coupled and hence encapsulate the complete cyclic oscillation of the instability mode. As detailed in Oberleithner *et al.* (2011) these modes can be utilised to comprehensively express the oscillating flow field through spatial reconstruction. Figures 13(*d*) and 13(*e*) show the energy distribution for the first axial POD mode for NPR 2.6 and NPR 3, respectively. Strong coupling effects along the inner shear layers are evident at both conditions. Additionally, the variations in the oscillation phase clearly align with the results observed in the SPOD analysis with the jets undergoing phase offset oscillations at NPR 2.6 and phase matched oscillations at NPR 3 along the inner shear layers. The triple decomposition technique formulated by Hussain & Reynolds (1970) was utilised to isolate the coherent component from the flow using

$$u\,(x,t) = \overline{u}\,(x) + u''(x,t) + u_c(x,t),\tag{3.2}$$

where u is the time varying velocity field $\overline{u}$ is the temporal average, u'' is the fluctuating component and u_c is the coherent component. Alternatively, the coherent flow component can also be represented using the first two POD modes (Edgington-Mitchell *et al.* 2014). To identify the various states of fluctuation velocity reconstruction was performed using the first two POD modes from the axial and radial components. The velocity contours were passed through a cross-correlation based image filter to isolate images at a singular fluctuation phase to emulate phase locking (Alkislar *et al.* 2003) as discussed in Appendix B. These filtered velocity components were then utilised to compute the coherent velocity fluctuations and directional streamlines illustrated in figure 14. The colour bar indicates the range of this magnitude. The streamlines were computed using the axial and radial coherent velocity fluctuations. An algorithm was developed to overlay the coherent velocity magnitude computed using

$$U_c = \sqrt{u_{rec}^2 + v_{rec}^2}\tag{3.3}$$

on top of the streamlines. In (3.3), u_{rec} and v_{rec} are the coherent velocity fluctuations in the axial and radial directions, respectively.

For NPR 2.6, peak fluctuations manifested just beyond the first shock cell, accompanied by vortical formations as depicted by the streamlines in figure 14(*a*). The vortices remained within the bounds of the shear layers, avoiding extension into the internozzle area, due to the phase differences between oscillations along the inner shear layers. This manifested as minimal velocity distributions along the nozzle symmetry line. Similar vortical formations were observed along the outer shear layers, intensifying post the first shock cell and progressing downstream. These formations tend to shift towards the jet core, influenced by transverse velocity fluctuations, as indicated by the R_{yy} stress component previously discussed.

Conversely, NPR 3 experiences stronger coherent fluctuations, fuelled by synchronised oscillations characteristic of this operational state. Notably robust vortical areas were detected following the first shock cell, affirming insights from the SPOD analysis, as shown in figure 14(*b*). Additionally, the formations emerging along the inner shear layers gradually drift towards the nozzle symmetry line, propelled by significant transverse fluctuations. This movement and the resultant hydrodynamic oscillations likely contribute to the branched pattern seen in the turbulence and Reynolds stress distributions in figure 13. These formations exhibit swift dissipation after $X/h = 4$, correlating with the observed decline in turbulence within the TKE profiles. A key insight from these observations is that the interplay between the first shock cell and coherent structures
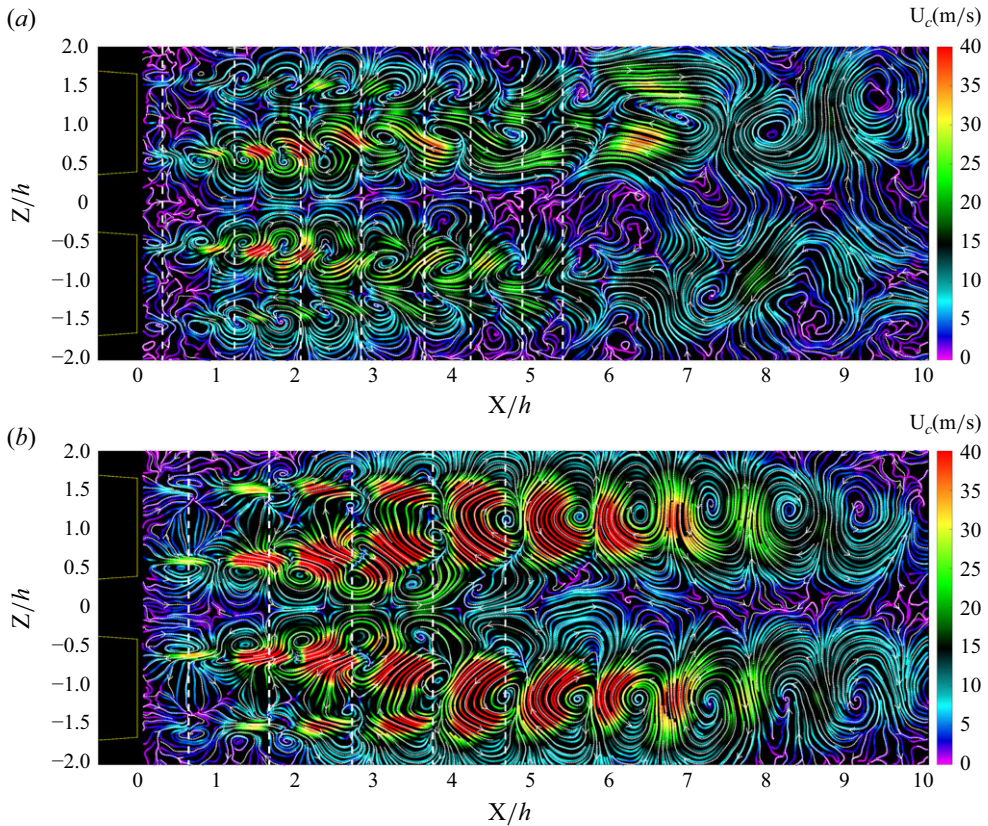
Figure 14. Streamlines of binned coherent velocities coloured with coherent velocity magnitude: (*a*) NPR 2.6; (*b*) NPR 3. Dashed lines indicate locations of shock inflection points. View normal to Twinjet plane.

initiates vortical formations pivotal for instability proliferation in screeching jets, with the amplitude of flow oscillations impacting their size and axial span.

4. Concluding remarks

Tam & Thies (1993) utilised vortex sheet formulation to analyse the mode preferences of rectangular jets. Their findings indicated that circular and square jets exhibited identical characteristics for pressure eigen functions ($|p|$) that govern the mode and type of instabilities. They observed that the propagation characteristics and pressure eigen function distribution of specific instability modes were sensitive to Strouhal number ($St_h = \omega h / u_j$, where ω is the angular frequency, h is the nozzle height and u_j is the exit velocity). Furthermore, the higher-order modes $|p|$ of a square jet closely resembled that of a circular jet. While these findings were for a purely convergent nozzle, they indicate that instability conditions in square nozzles can be similar to those observed in circular nozzles. This is particularly evident in the far-field azimuthal distribution of the fundamental screech tone in the Symmetry plane ((3.1), figure 2) that bears a strong resemblance to the pattern of instability propagation for circular jets recorded by Norum (1983).

Tam & Thies (1993) also identified the four distinct instability families for rectangular jets, illustrated in figure 15, each comprising an infinite series of modes. Among these,
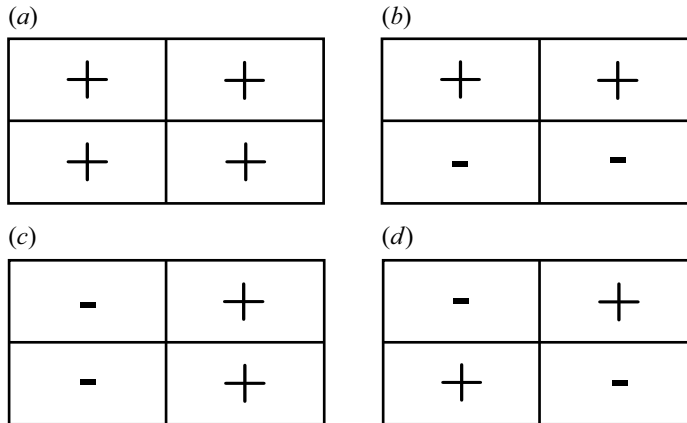
Figure 15. The four families of symmetric and antisymmetric instabilities found in rectangular jets: (*a*) family 1, (*b*) family 2, (*c*) family 3 and (*d*) family 4. This figure is identical to figure 7 of Tam & Thies (1993).

the first and third mode were identified as corner modes encompassing highly localised flow fluctuations that occur in the jet's corner regions. Conversely, the second/centre mode captures flow oscillations in the jet core and was noted as having the largest spatial growth rate, which remained unaffected by the jet Mach number. This higher growth rate in the downstream direction made it the dominant oscillation mode. The combination of these modes within each instability family influences the jets fluctuation pattern. The similarity in the distribution of |*p*| between circular and square jet for the centre mode could lead to the dominant oscillation emerging family 1 or family 2 with comparable probability.

This is unlike rectangular jets where the centre mode from family 2 featured consistent prominence independent of the Mach number or AR. Coupled with the instability sensitivity to Mach number, these findings support the observed oscillation behaviour of twin square jets. The coherent vortices detected in the current study are indicative of the oscillation preference of screeching jets and are persistent along the shear layers that experience the highest fluctuation amplitude. The vortices originate from small-scale *KH* instabilities within the shear layer growing through a process similar to collective interaction proposed by Ho & Nassier (1981). However, unlike the mechanism in imping-ing jets where the subharmonic growth that fosters collective interaction is constrained by jet impingement, the process continues in free jets. The detection of the subharmonic frequency peak observed in the LST noise supports this hypothesis (Appendix A). The progression of this mechanism leads to shear layer thickening and the persistent growth of the coherent structures. Additionally, interactions between the coherent structures and shock tips furthers their growth as seen in figure 14 (also illustrated in Appendix D). The expansion rate of these structures hinges on the jet's preferred instability mode and the excitation frequency of the G-JM that enables screech closure.

This research was dedicated to exploring the complexities of flow dynamics exhibited by twin supersonic square jets in unstable operational states. The study aimed to delineate various oscillation modes of the jets by utilising spectral decomposition methods to identify the underlying mechanisms. In the overexpanded operational regime, two distinct instability modes were observed. At NPR 2.6, the jets displayed out-of-phase oscillations within the inner shear layers, significantly diminishing interaction components and turbulence along the nozzle symmetry line. The generation of the primary instability tone was attributed to a G-JM arising from the triadic interaction between the initial shock cell

and *KH* instabilities. At NPR 3, the jets exhibited phase-locked oscillations along the inner shear layers, propelled by triadic interactions that facilitated a G-JM, thereby sustaining the feedback loop essential for screech fluctuations. Across both operating conditions, the first harmonic was generated as a result of shock–turbulence interactions between the *KH* instabilities with the second shock cell. However, these suboptimal interaction did not produce any discernible G-JM signatures. For both scenarios, the first harmonic demonstrated phase-locked oscillations within the inner shear layers.

Turbulence energy concentrations at NPR 2.6 were markedly pronounced along the outer shear layers, with a noticeable reduction along the nozzle symmetry line, influenced by the destructive interference within the inner shear layers. Conversely, at the higher NPR, pronounced symmetric oscillations fostered a branched turbulence profile extending from the inner shear layer towards the nozzle symmetry plane, propelled by transverse fluctuations in the Twinjet plane. Additionally, the study revealed through POD mode reconstruction that the interaction with the first shock cell is pivotal in the early stages of coherent structure formation, subsequently leading to vortical formations along the jet shear layers. The strength and axial locations of these vortices show a clear dependence on the instability fluctuation amplitude.

A notable similarity between the current study and the findings of Karnam *et al.* (2023) is the distinct behaviour of the jets at NPR 2.6. Due to the comparable design operating conditions of the present nozzle and the rectangular nozzle studied by Karnam *et al.* (2023), both jets exhibit pronounced multimode behaviour at NPR 2.6, characterised by the formation of clear standing waves across all jet shear layers, as shown in figure 3(*b,c*). This is an indication of simultaneous varicose fluctuation propagating along all the jet shear layers. These findings underscore the critical role nozzle design parameters play in shaping the instability characteristics of supersonic jets. Consequently, the design space of these supersonic nozzles emerges as a significant factor in influencing unstable jet behaviour. Additionally, the current study highlights the role of the quasisteady shock structure of a supersonic jet in the generation and propagation of unstable jet modes.

Data availability. The data that support the findings of this study are available from the corresponding author upon reasonable request.

Author contributions. A.K. – conceptualisation (equal), formal analysis (lead), investigation (lead), methodology (lead), resources (equal), validation (lead), writing of original draft (lead). M.A. – conceptualisation (equal), formal analysis (equal), investigation (equal),methodology (equal), validation (equal), writing of review and editing (equal). M.M. – conceptualisation (equal), investigation (equal), supervision (lead), writing of review and editing (equal). M.S. – investigation (equal), formal analysis (equal), writing of review and editing (support). E.G. – conceptualisation (equal), investigation (equal), supervision (equal), writing of review and editing (equal), resources (lead), funding acquisition (lead).

Conflict of interest. The authors have no conflicts to disclose.

Appendix A. Supplementary acoustic spectra

Figure 16 depicts the acoustic frequency spectra from downstream observer angles discussed in § 3. At NPR 2.6, the screech frequency at $St \approx 0.51$ (10.4 kHz) showed strong peaks at $\xi = 126°$ and $\xi = 148°$ in the Symmetry plane. Conversely, in the Twinjet plane, this frequency peaked at $\xi = 126°$ and $\xi = 144°$.
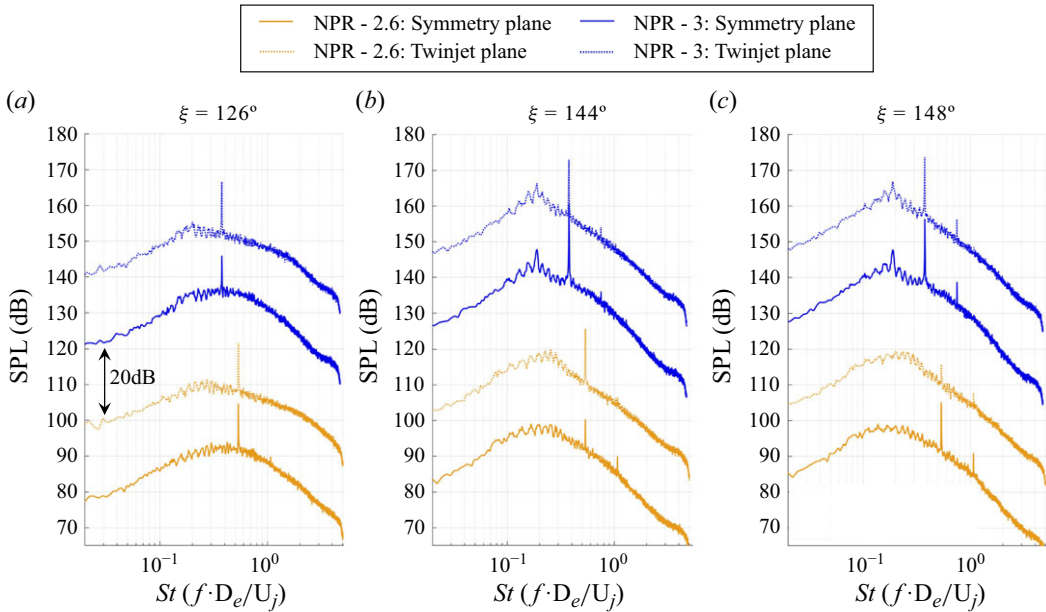
Figure 16. Frequency spectra for NPR 2.6 (gold) and NPR 3 (blue) at three different azimuthal angles: (*a*) $\xi = 126°$; (*b*) $\xi = 144°$; (*c*) $\xi = 148°$. The spectra are separated by a step size of 20 dB. Results from the Symmetry plane are plotted with solid lines and results from the Twinjet plane are plotted with dotted lines. Note the variation in screech peaks at the lower angle.

On the other hand, at NPR 3 the screech frequency at $St \approx 0.38$ (8.15 kHz) showed consistent peaks at $\xi = 144°$ and $\xi = 148°$ across both observation planes accompanied by a sharper profile of the LST peak at $St \approx 0.19$ (4.1 kHz). This frequency matches the subharmonic screech frequency indicating that the symmetric flapping mode results in consistent production of large coherent structures in addition to the *KH* instabilities that are a major contributor to the LST noise component.

Appendix B. Spatial decomposition methodology

To isolate the various spatial components coupled with the instability tones of the nozzles a spatial decomposition algorithm based on the work of Edgington-Mitchell *et al.* (2021, 2022) was implemented. While their studies used the dominant modes from POD and dynamic mode decomposition of screeching jets, respectively, in the current study the results of the temporal Fourier decomposition at the screech frequency were used as an input for the algorithm as shown,

$$\psi = \hat{I}_\omega e^{-i\omega t} \tag{A1}$$

$$\hat{\psi}_k^\omega(y) = \sum \psi(x, y)e^{-ikx} \tag{A2}$$

$$\psi_k'(x, y) = \sum_{k_1}^{k_2} \hat{\psi}_k^\omega(y)\, e^{-ikx}, \tag{A3}$$

where ψ is the temporal Fourier term associated with the frequency of interest ω and $\hat{\psi}_k^\omega(y)$ is the streamwise spatial Fourier transform computed at each radial location converting the energy distribution from the spatial-frequency domain into the
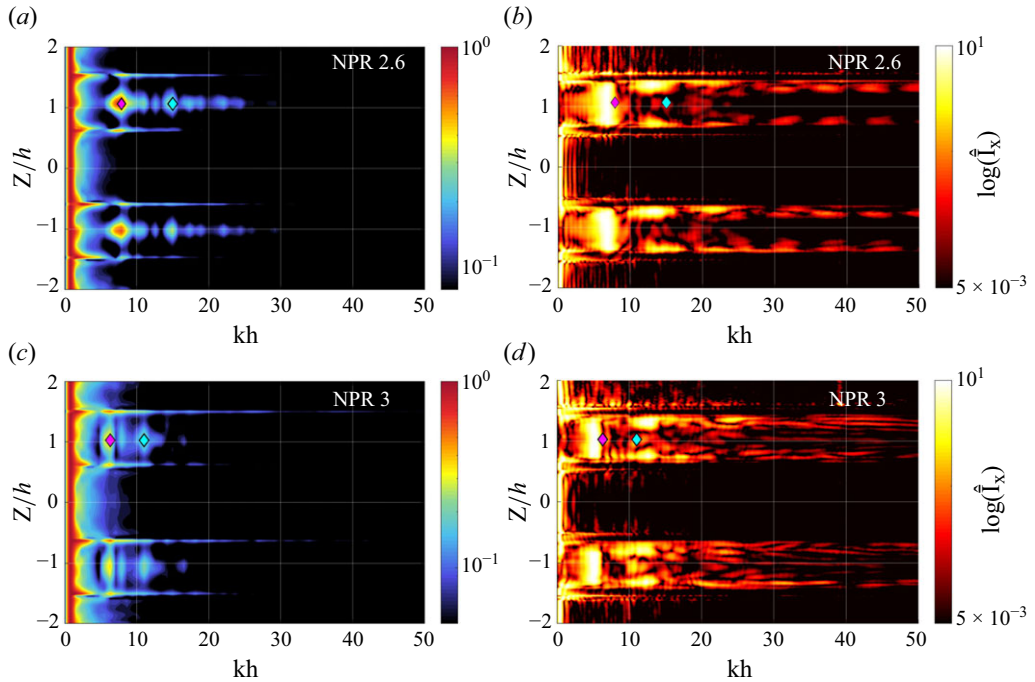
1009 A13-29

Figure 17. Fourier spatial decomposition obtained from average axial velocity profile and schlieren images to identify shock cell wavenumbers. (*a,b*) NPR 2.6: (*a*) axial velocity from PIV images; (*b*) average schlieren image decomposition. (*c,d*) NPR 3: (*c*) axial velocity from PIV images; (*d*) average schlieren image decomposition. Magenta, first shock cell wavenumber; cyan, second shock cell wavenumber.

spatial-wavenumber domain. The positive wavenumbers identify waves propagating in the downstream direction, while the negative wavenumbers identify those travelling towards the jet upstream. The energy distributions obtained from spatial Fourier transformations can be used to reconstruct spatial energy distributions associated with singular wavenumbers as shown by (A3).

Where $\psi'_k(x, y)$ represents the spatial distribution of energy associated with the centre wavenumber k and is obtained through the inverse Fourier transform reconstructed over the wavenumber range $[k_1 \ k_2]$. To achieve this, a Kaiser window with a half-width of $1.9h$ centred on k was employed to the domain limits. To account for the limited spatial resolution of the source images, some interpolation was applied to identify the wavenumber that is closest to the interaction wavenumbers discussed in §3.2. This methodology was applied to the temporal average of the axial velocity distribution from PIV and the temporal average of the schlieren images. The analysis results are illustrated in figure 17 for both jet operating conditions. The magenta marker indicates the wavenumber of the first shock cell, while the cyan marker indicates that of the second shock cell. A deviation between the wavenumbers derived from the PIV data and schlieren data was observed, as summarised in table 3.

This variation can be attributed to two primary factors. First, the intricate nature of the shock cell system in square jets, as described by Zhang *et al.* (2017), can cause significant deviations in the light passing through the jet. Since the camera captures an integrated average of the light traversing this complex shock structure, such variations are not unexpected. Additionally, the throat shock structure introduces further light path deviations from the shock train, leading to the wavenumber disparity compared with the

NPR	k_{S1}, PIV	k_{S1}, schlieren	Δk_{S1}
2.6	7.88	6.73	1.15
3	6.31	5.35	0.96

Table 3. Shock cell wavenumbers.

PIV results. The second factor relates to the acquisition method of the PIV images, which were obtained from the jet's centre plane. This approach avoids the path integration effects inherent in schlieren imaging, resulting in data that represents a shallower point plane and, consequently, exhibits lower positional deviation of the shock cells. Considering these factors, subsequent analyses primarily utilise the wavenumbers derived from the schlieren measurements.

Appendix C. Validation and supplementary flow field results

The experimental TKE described in § 3.4 is computed using

$$TKE = \frac{0.5(u'^2 + 2v'^2)}{U_j{}^2} \tag{A4}$$

where, u' is the fluctuating component of the axial velocity and v' is the fluctuating component of the radial velocity and U_j is the isentropic exit velocity. As the experimental data does not capture the out of plane velocity components, they are accounted for by a second radial velocity fluctuation term. Previous studies by Baier, Karnam & Gutmark (2020) and Chakrabarti *et al.* (2022) demonstrated that this approach captures the turbulence levels with reasonable accuracy. The Reynolds stresses are computed using (A6), where u'_i and v'_i are the fluctuating axial and radial velocity field in the i th sample:

$$R_{u,v} = cov\,(u,\,v) = \frac{1}{N-1} \sum_{i=1}^{N} u'_i \cdot v'_i. \tag{A5}$$

Here N is the total number of samples; R_{xx} and R_{yy} stress fields are computed using identical field pairs (e.g. for $R_{xx}: u' \cdot u'$, etc.). Velocity uncertainty was computed over the sampling range of 2400 images based on the methodology of Lazar *et al.* (2010).

The uncertainty was computed using

$$\varepsilon = \bar{u} \pm z \frac{\sigma}{N}, \tag{A6}$$

where, $\bar{u}$ is the mean velocity value, σ is the standard deviation for the velocity field, z is the Z-score and N is the total number of samples. The peak uncertainty values for NPR 3 in the axial velocity field was ± 3.48 m s^{-1} for a 95 % confidence interval ($z = 1.96$) and ± 4.57 m s^{-1} for a 99 % confidence interval ($z = 2.576$). In the case of the radial velocity field, these values were recorded at ± 2.32 ms^{-1} (95 % confidence) and ± 3 m s^{-1} (99 % confidence). These values are comparatively lower than those from Jeun *et al.* (2022) ensuring data accuracy.

To ensure that the sample set was statistically invariant (stationary in the time sense), uncertainty values were computed for increasing sample sizes ($N_{i+1} = N_i + 5$) using a random set of images as illustrated in figure 18. Figure 18(a) shows the distribution of these uncertainties. A clear exponential reduction was observed in the peak and mean
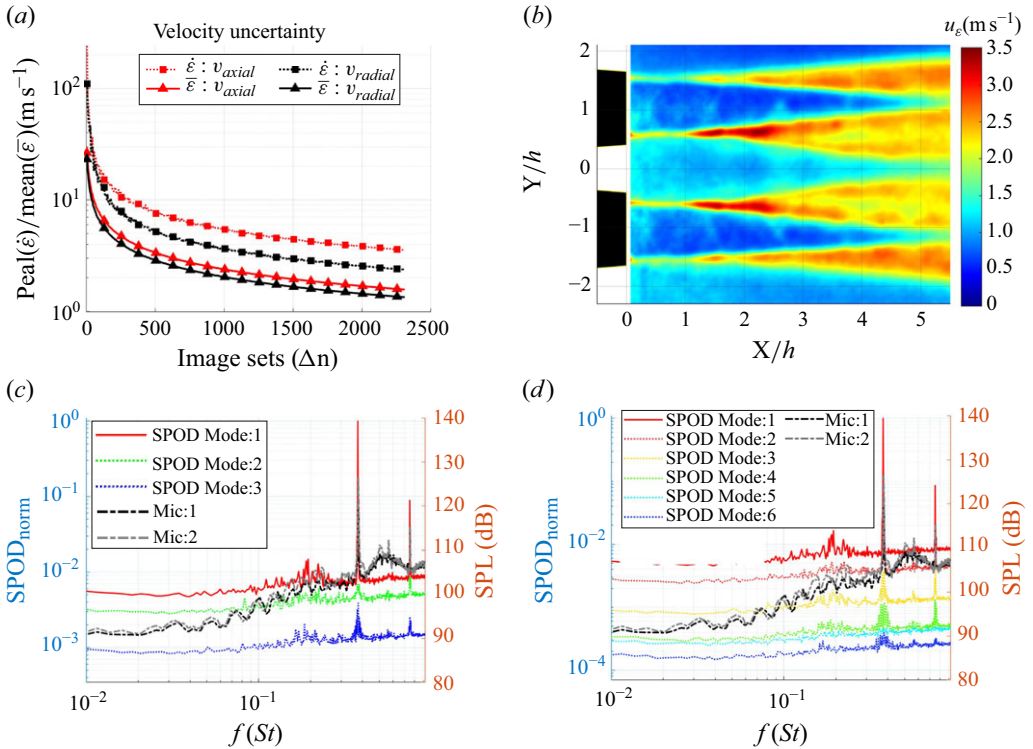
Figure 18. (*a*) Peak uncertainty across multiple random image sets. (*b*) Uncertainty distribution in axial velocity field ($N = 2400$ samples). Comparison of SPOD peak energy with near field acoustic for NPR 3, (*c*) The 50 % FFT image block overlap. (*d*) The 75 % FFT image block overlap.

uncertainty values across both axial and radial velocities. The curves approach asymptotic behaviour close to $N = 2400$ indicating the sample size was large enough to ensure accuracy in the velocity field measurement. Figure 18(*b*) illustrates the uncertainty map for the first camera location where the peak values were measured. The location of the uncertainty peak in the shear layers indicates that the shock-expansion locations were measured with reliable accuracy.

Additionally, the peak value of ± 3.48 m s^{-1} observed at X/$h = 2.23$ translates to only 1.3 % variation in the mean velocity at that location. To assess the convergence of the SPOD results two computations were conducted with varying degree of overlap. The results from these analyses are presented in figure 18(*c,d*) for the case of NPR 3. Overlaid on the SPOD energy distribution plot is the near field acoustics result that was obtained simultaneously with the schlieren images. Across both overlap conditions the location of the peak instability frequency and the harmonic align with the instability frequencies from the near field acoustics. This demonstrates a clear convergence in the SPOD frequencies. To validate modal convergence SPOD analysis was conducted on three data configurations for the condition of NPR 3. The first configuration utilises the complete image set ($N_T = 2000$) with a block size (N_{F1}) of 820 snapshots with 75 % overlap between blocks yielding a frequency resolution of 50 Hz. The second configuration also utilised the compete image set with a reduced block size of 210 snapshots resulting in a frequency resolution of 200 Hz. The third configuration consisted of a half of the image set (1000 snapshots) with a block size of 410 snapshots resulting in a frequency resolution of 100 Hz. These configurations were designed to cover combinations of frequency resolution, data
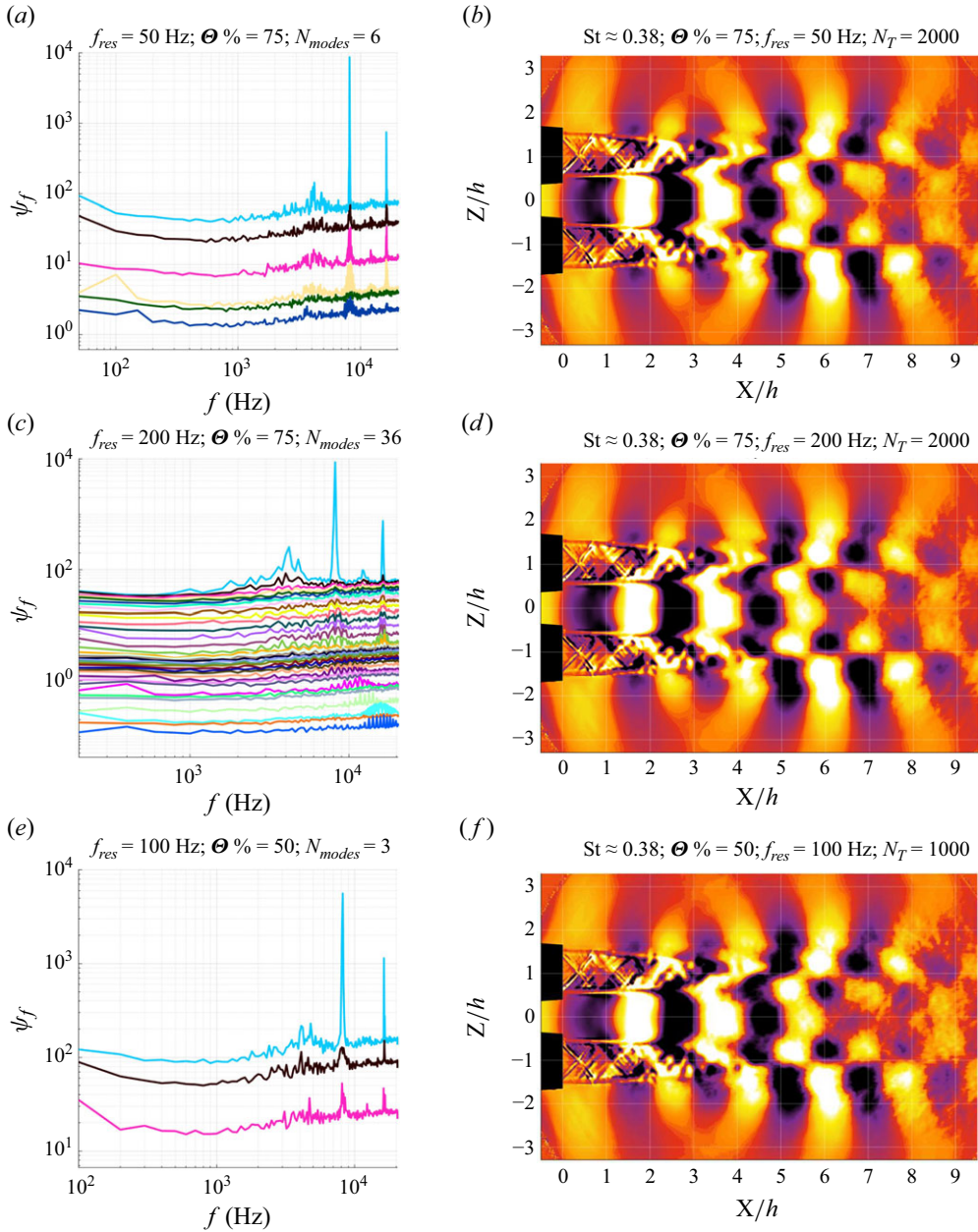
Figure 19. The SPOD mode convergence analysis for NPR 3. (a,c,e) The SPOD mode energy distribution. (b,d,f) Spatial mode energy distribution at peak screech frequency of st ≈ 0.38. Here (a,b) $N_T = 2000$, $f_{res} = 50Hz$, block overlap $(\Theta \%) = 75$; (c,d) $N_T = 2000$, $f_{res} = 200Hz$, block overlap $(\Theta \%) = 75$; (e,f) $N_T = 1000$, $f_{res} = 50Hz$, block overlap $(\Theta \%) = 50$.

snapshot range and block overlap percentage. Figure 19 illustrates the results from the analysis. Although significant variation in the mode distribution was observed driven by block size and frequency resolution, the modal energy distribution remained unchanged as illustrated by the energy distribution maps in figure 19(b,d,f) across all conditions. This consistency provides a clear indication of model energy convergence.
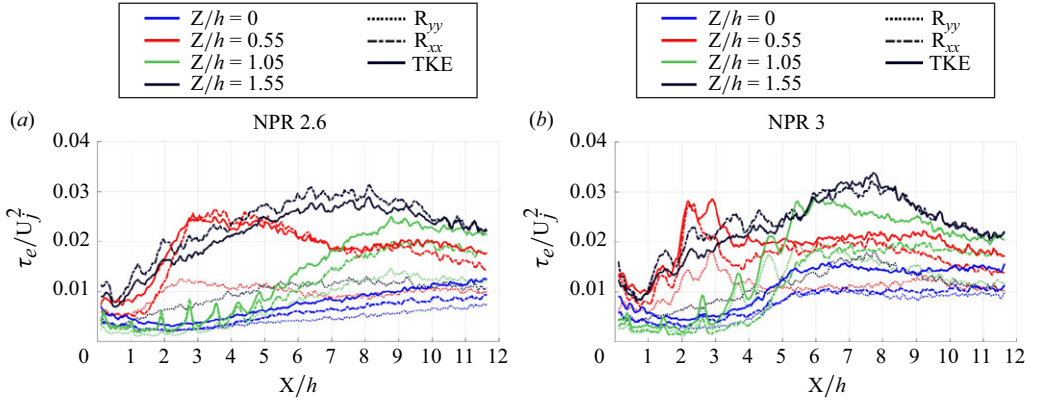
Figure 20. Profiles of normalised turbulence quantities (τ_e) along the axial direction at four distinct radial locations: (*a*) NPR 2.6; (*b*) NPR 3. Both plots are for experimental data and are obtained from the upper jet.

The trends presented in figure 20 show distributions of turbulence quantities, TKE and Reynolds stresses, along the nozzle symmetry line (blue) and shear layers. While the outer shear layers generally dominate as the locations with the overall peak energy level across both conditions, NPR 3 showed a sharp increase in the centreline turbulence levels after $X/h = 4$ driven by the stronger flow fluctuations at these conditions. The energy branching along the inner shear layer at NPR 3 leads to local spikes in turbulence shortly after the first shock cell along the inner shear layers (red) as seen in figure 20(*b*). This is driven by the intensification of flow fluctuations after interaction with the first shock cell.

Also notable is the peak turbulence level along the centreline (green) matching the values observed along the outer shear layer at $X/h = 6$ powered by the transverse fluctuations that cause large perturbations in the flow.

Appendix D. The POD based reconstruction methodology

The POD based on the methodology of Oberleithner *et al.* (2011) and Edgington-Mitchell *et al.* (2014) was adopted for this study and is briefly discussed below. The fluctuating velocity components from the flow data (axial and radial velocity) consisting of N individual snapshots were computed using

$$u'(x, t_k) = u(x, t_k) - \overline{u}(x, t), \tag{A7}$$

where u' is the fluctuating velocity field of the kth snapshot ($k = 1, 2, 3. \ldots N$) and $\overline{u}$ is the temporal average. The goal of the decomposition is to represent the fluctuating velocity field as a collection of least-order representations while minimising the residual energy expressed as

$$u'(x, t_k) = \sum_{j=1}^{N} a_j(t_k) + \varphi_j(x) + u_r(x, t_k). \tag{A8}$$

Here a_j is the temporal coefficient associated with the spatial distribution φ_j for the jth mode while satisfying the criteria $u_r \to 0$. The algorithm introduced by Sirovich (1987) based on an autocorrelation matrix is implemented as follows:

$$R = U^T U \tag{A9}$$

to compute the autocorrelation matrix R of order $N \times N$ for the velocity snapshot matrix U. This can be reformulated into an eigenvalue problem represented as

$$Ra_j = \lambda_j a_j \tag{A10}$$

where λ_j is the eigenvalue corresponding to twice the TKE of the jth mode arranged in descending order. The corresponding eigenvector, a_j can be used to compute the spatial modes using

$$\varphi_j(x) = \frac{1}{\sqrt{N\lambda_j}} \sum_{j=1}^{N} a_j(t_k) \cdot u'(x, t_k). \tag{A11}$$

The required velocity profiles can then be reconstructed from the spatial energy modes using

$$u'_{rec}(x, t) = \sum_{m=1}^{M} \varphi_m(x) \cdot a_m(t_m) \tag{A12}$$

where u'_{rec} is the reconstructed velocity field derived from m spatial modes. A cross-correlation filter was then applied to the reconstructed data set denoted as follows to filter phase matched velocity snapshots:

$$\hat{R}_{x,x}(y_i) = E\left\{u_x(y_i, t_n) \cdot u_x(y_i, t_k)^*\right\}. \tag{A13}$$

Here, $\hat{R}_{x,x}$ denotes the cross-correlation of axial velocity (u_x) at a specified radial location y_i, comparing a reference frame (n) to the kth velocity snapshot. E denotes the expectation operator and $*$ represents the complex conjugate. The data filtering process spanned across all reconstructed axial velocity snapshots by utilising the velocity distribution close to the nozzle lip line from a reference frame. Snapshots meeting the phase matching criteria of $\hat{R}_{x,x} > 0.99$ were selected. These selected axial velocity snapshots, in combination with the corresponding radial velocity snapshots were utilised to compute the coherent velocity fluctuations and the corresponding streamlines.

Figure 21 displays the outcomes of velocity reconstruction and filtering using the first two POD modes. The diagrams illustrate streamlines and vorticity profiles derived from the reconstruction and phase-binning procedure described above. The planar vorticity profiles were computed from the curl of velocity field (represented by $\vec{v} = u\hat{i} + v\hat{j}$ where u is the axial velocity and v is the radial velocity) from the Twinjet plane (XZ plane) using

$$\omega = \nabla \times \vec{v} = \frac{\partial v}{\partial x} - \frac{\partial u}{\partial y} \tag{A14}$$

where ω is the planar vorticity with the axis of rotation pointing out of the image plane towards the reader.

Streamlines computed using the magnitude of coherent velocity fluctuation and coloured by normalised vorticity magnitudes ($|\omega| \cdot h/U_j$) are illustrated in figure 21(a,c). While the figure 21(b,d) illustrates the streamlines computed using the instantaneous reconstructed velocity components that are coloured with the instantaneous velocity magnitude. At NPR 2.6, shear forces outside the nozzle exit lead to the formation of instability vortices. These coherent vortices appear to be energised after interacting with the first shock cell as indicated by the peak vorticity magnitude at X/h = 1.1 across both shear layers in figure 21(a). This also results in the generation of a weaker vortices along the inner shear layers as illustrated in figure 21(b). Due to the phase mismatch between the inner shear layers at this condition, there were no identifiable vortices observed in the
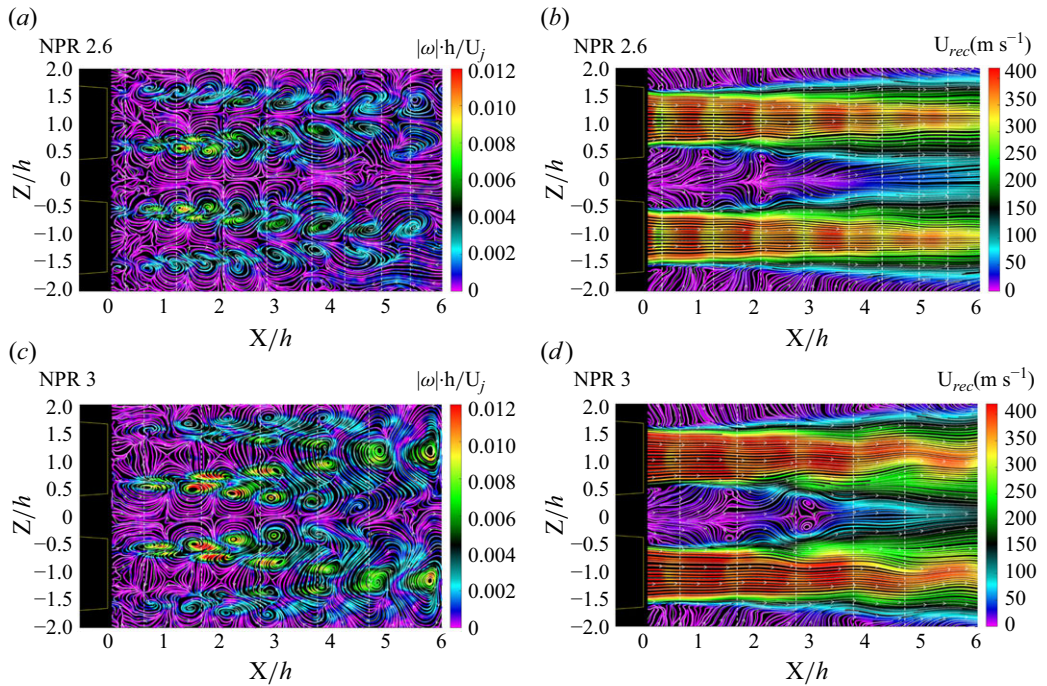
Figure 21. Planar vorticity ($\nabla \times \mathbf{F}(u, v)$) and binned velocity profile reconstructions. Streamlines were computed from the filtered axial(u) and radial (v) velocity profiles of the PIV dataset and are coloured with instantaneous velocity magnitudes: (*a,b*) NPR 2.6; (*c,d*) NPR 3. Dotted lines represent shock inflection points. View normal to Twinjet plane.

internozzle region reinforcing the conclusions drawn from the schlieren image analysis in § 3.2.

The phase matched velocity magnitudes indicate the formation of two prominent vortical regions close to the first and second shock cells. These observations resemble the findings by Alkislar *et al.* (2003) where large vortices were observed close to local Reynolds stress peaks in the shear layers of an AR 4 screeching rectangular jet. At NPR 3, the experimental findings revealed stronger vortex formations in the shear layer adjacent to the first and second shock cells, as shown in figure 21(*c*). Interestingly, two families of vortices were identified with locations matching the turbulence branching feature observed in figure 13. The strong symmetrical oscillations in the jets at these conditions drive the one set of vortices closer to the symmetry plane while the second set is driven closer to the jet core. The inner shear layer vortex cores proceed to merge with the vortices from the outer shear layers close to $X/h = 5$. This location precisely aligns with the merging point of the shear layers observed in the TKE profile in § 3.4, figure 12(*b*). Additionally, the vortices that migrate towards the symmetry line manifest in the phase matched total velocity profile as illustrated in figure 16(*d*). The locations of the two vortices match precisely with the turbulence peak along the inner shear layers at $X/h = 2$ and the turbulence branch that initiates at $X/h = 3$.

REFERENCES

AHN, M., KARNAM, A., GUTMARK, E. & MIHAESCU, M. 2021a Flow and near-field pressure fluctuations of twin square jets. In *AIAA Propulsion and Energy 2021 Forum*. American Institute of Aeronautics and Astronautics, virtual event.

AHN, M., LEE, D.-J. & MIHAESCU, M. 2021b A numerical study on near-field pressure fluctuations of symmetrical and anti-symmetrical flapping modes of twin-jet using a high-resolution shock-capturing scheme. *Aerosp. Sci. Technol.* **119**, 107147.

AHN, M., MIHAESCU, M., KARNAM, A. & GUTMARK, E. 2023 Large-eddy simulations of flow and aeroacoustics of twin square jets including turbulence tripping. *Phys. Fluids* **35** (6), 066105.

ALKISLAR, M.B., KROTHAPALLI, A. & LOURENCO, L.M. 2003 Structure of a screeching rectangular jet: a stereoscopic particle image velocimetry study. *J. Fluid Mech* **489**, 121–154.

ANAND, V., JODELE, J., SHAW, V., RUSSELL, A., PRISELL, E., LYRSELL, O. & GUTMARK, E. 2021 Visualization of valved pulsejet combustors and evidence of compression ignition. *Flow Turbulence Combust* **106** (3), 901–924.

ANDRÉ, B., CASTELAIN, T. & BAILLY, C. 2014 Investigation of the mixing layer of underexpanded supersonic jets by particle image velocimetry. *Intl J. Heat Fluid Flow* **50**, 188–200.

BAIER, F., KARNAM, A. & GUTMARK, E. 2020 Cold flow measurements of supersonic low aspect ratio jet-surface interactions. *Flow Turbulence Combust* **105** (1), 1–30.

BELL, G., CLUTS, J., SAMIMY, M., SORIA, J. & EDGINGTON-MITCHELL, D. 2021 Intermittent modal coupling in screeching underexpanded circular twin jets. *J. Fluid Mech.* **910**, A20.

BELL, G., SORIA, J., HONNERY, D. & EDGINGTON-MITCHELL, D. 2018 An experimental investigation of coupled underexpanded supersonic twin-jets. *Exp. Fluids* **59** (9), 139.

CHAKRABARTI, S., GAITONDE, D.V., UNNIKRISHNAN, S.NAIR, STACK, C., BAIER, F., KARNAM, A. & GUTMARK, E. 2022 Turbulent statistics of a hot, overexpanded rectangular jet. *J. Propul. Power* **38** (3), 421–436.

CHEN, S., GOJON, R. & MIHAESCU, M. 2021 Flow and aeroacoustic attributes of highly-heated transitional rectangular supersonic jets. *Aerosp. Sci. Technol.* **114**, 106747.

DUSA, D., SPEIR, D., ROWE, R. & LEAVITT, L. 1983 Advanced technology exhaust nozzle development. In *19th Joint Propulsion Conference*. American Institute of Aeronautics and Astronautics.

EDGINGTON-MITCHELL, D. 2019 Aeroacoustic resonance and self-excitation in screeching and impinging supersonic jets – a review. *Intl J. Aeroacoust.* **18** (2–3), 118–188.

EDGINGTON-MITCHELL, D.M., BEEKMAN, J. & NOGUEIRA, P. 2022 Screech mode staging in rectangular and elliptical jets. In *28th AIAA/CEAS Aeroacoustics 2022 Conference*. American Institute of Aeronautics and Astronautics.

EDGINGTON-MITCHELL, D., HONNERY, D.R. & SORIA, J. 2015 Staging behaviour in screeching elliptical jets. *Intl J. Aeroacoust.* **14** (7), 1005–1024.

EDGINGTON-MITCHELL, D., JAUNET, V., JORDAN, P., TOWNE, A., SORIA, J. & HONNERY, D. 2018 Upstream-travelling acoustic jet modes as a closure mechanism for screech. *J. Fluid Mech.* **855**, R1.

EDGINGTON-MITCHELL, D., LI, X., LIU, N., HE, F., WONG, T.Y., MACKENZIE, J. & NOGUEIRA, P. 2022 A unifying theory of jet screech. *J. Fluid Mech.* **945**, A8.

EDGINGTON-MITCHELL, D., OBERLEITHNER, K., HONNERY, D.R. & SORIA, J. 2014 Coherent structure and sound production in the helical mode of a screeching axisymmetric jet. *J. Fluid Mech.* **748**, 822–847.

EDGINGTON-MITCHELL, D., WANG, T., NOGUEIRA, P., SCHMIDT, O., JAUNET, V., DUKE, D., JORDAN, P. & TOWNE, A. 2021 Waves in screeching jets. *J. Fluid Mech.* **913**, A7.

EDGINGTON-MITCHELL, D., WEIGHTMAN, J., LOCK, S., KIRBY, R., NAIR, V., SORIA, J. & HONNERY, D. 2021 The generation of screech tones by shock leakage. *J. Fluid Mech.* **908**, A46.

GOJON, R., GUTMARK, E. & MIHAESCU, M. 2019 Antisymmetric oscillation modes in rectangular screeching jets. *AIAA J.* **57** (8), 3422–3441.

GUTMARK, K.C.SCHADOW & BICKER, C.J. 1990 Near acoustic field and shock structure of rectangular supersonic jets. *AIAA J.* **28** (7), 1163–1170.

HARPER-BOURNE, M. & FISHER, M.J. 1973 The noise from shock waves in supersonic jets. In *Proceesings of Noise Mechanisms*, pp. 11–13. NATO.

HEEB, N.S., SANCHEZ, P.MORA, GUTMARK, E.J. & KAILASANATH, K. 2013 Investigation of the noise from a rectangular supersonic jet. In *19th AIAA/CEAS Aeroacoustics Conference*. American Institute of Aeronautics and Astronautics.

HO, C.-M. & NOSSEIR, N.S. 1981 Dynamics of an impinging jet. Part 1. The feedback phenomenon. *J. Fluid Mech.* **105** (1), 119.

HUSSAIN, A.K.M.F. & REYNOLDS, W.C. 1970 The mechanics of an organized wave in turbulent shear flow. *J. Fluid Mech.* **41** (2), 241–258.

JEUN, J., KARNAM, A., WU, G.JUN, LELE, S.K., BAIER, F. & GUTMARK, E.J. 2022 Aeroacoustics of twin rectangular jets including screech: large-eddy simulations with experimental validation. *AIAA J.* **60** (11), 6340–6360.

JEUN, J., WU, G.J. & LELE, S.K. 2022 A closure mechanism for screech coupling in rectangular twin jets. arXiv:2210.11567

KARNAM, A., AHN, M., GUTMARK, E. & MIHAESCU, M. 2022 Effects of screech on jet coupling in twin square jets. In *28th AIAA/CEAS Aeroacoustics 2022 Conference*. American Institute of Aeronautics and Astronautics.

KARNAM, A., SALEEM, M. & GUTMARK, E. 2023 Influence of nozzle geometry on screech instability closure. *Phys. Fluids* **35** (8), 086119.

KNAST, T., BELL, G., WONG, M., LEB, C.M., SORIA, J., HONNERY, D.R. & EDGINGTON-MITCHELL, D. 2018 Coupling modes of an underexpanded twin axisymmetric jet. *AIAA J.* **56** (9), 3524–3535.

KROTHAPALLI, A., BAGANOFF, D. & KARAMCHETI, K. 1981 On the mixing of a rectangular jet. *J. Fluid Mech.* **107** (1), 201.

KROTHAPALLI, A., HSIA, Y., BAGANOFF, D. & KARAMCHETI, K. 1986 The role of screech tones in mixing of an underexpanded rectangular jet. *J. Sound Vib.* **106** (1), 119–143.

KUO, C.-W., CLUTS, J. & SAMIMY, M. 2017 Exploring physics and control of twin supersonic circular jets. *AIAA J.* **55** (1), 68–85.

KUO, C.-W., MCLAUGHLIN, D.K., MORRIS, P.J. & VISWANATHAN, K. 2015 Effects of jet temperature on broadband shock-associated noise. *AIAA J.* **53** (6), 1515–1530.

LaVision GmbH. 2017 FlowMaster – Product Manual for DaVis 8.4. LaVision GmbH.

LAZAR, E., DEBLAUW, B., GLUMAC, N., DUTTON, C. & ELLIOTT, G. 2010 A practical approach to PIV uncertainty analysis. In *27th AIAA Aerodynamic Measurement Technology and Ground Testing Conference*. American Institute of Aeronautics and Astronautics.

LI, X., WU, X., LIU, L., ZHANG, X., HAO, P. & HE, F. 2023 Acoustic resonance mechanism for axisymmetric screech modes of underexpanded jets impinging on an inclined plate. *J. Fluid Mech.* **956**, A2.

LIANG, L.-L., WAN, Z.-H., YE, C.-C., ZHANG, P.-J.-Y., SUN, D.-J. & LU, X.-Y. 2023 Flow dynamics and noise generation mechanisms in supersonic underexpanded rectangular and planar jets. *AIP Adv.* **13** (6), 065128.

MALLA, B. & GUTMARK, E.J. 2017 Nearfield characterization of low supersonic single expansion ramp nozzles with extended ramps. In *55th AIAA Aerospace Sciences Meeting*. American Institute of Aeronautics and Astronautics.

MANCINELLI, M., JAUNET, V., JORDAN, P. & TOWNE, A. 2019 Screech-tone prediction using upstream-travelling jet modes. *Exp. Fluids* **60** (1), 22.

MANCINELLI, M., JAUNET, V., JORDAN, P. & TOWNE, A. 2021 A complex-valued resonance model for axisymmetric screech tones in supersonic jets. *J. Fluid Mech.* **928**, A32.

MANNING, T. & LELE, S. 2000 A numerical investigation of sound generation in supersonic jet screech. In *6th Aeroacoustics Conference and Exhibit*. American Institute of Aeronautics and Astronautics.

MARTIN, O.G., WU, G.J. & LELE, S.K. 2021 Coherence of screech generation at the 2nd harmonic for a rectangular jet. In *AIAA SCITECH. 2023 Forum*. American Institute of Aeronautics and Astronautics.

MITCHELL, D.M., HONNERY, D.R. & SORIA, J. 2013 Near-field structure of underexpanded elliptic jets. *Exp. Fluids* **54** (7), 1578.

MOHANTA, P.K. & SRIDHAR, B.T.N. 2017 Study of decay characteristics of hexagonal and square supersonic jet. *Intl J. Turbo Jet Eng.* **34** (2).

MONTERO, I.PADILLA, RODRIGUEZ, D., JAUNET, V., GIRARD, S., EYSSERIC, D. & JORDAN, P. Mean flow and linear stability analysis of twin supersonic jets. In *AIAA AVIATION. 2023 Forum*. American Institute of Aeronautics and Astronautics.

MUNDAY, D., GUTMARK, E., LIU, J. & KAILASANATH, K. 2011 Flow structure and acoustics of supersonic jets from conical convergent-divergent nozzles. *Phys. Fluids* **23** (11), 116102.

NGUYEN, T., MAHER, B. & HASSAN, Y. 2020 An experimental investigation of a square supersonic jet and impinging jet on an inclined plate. *AIP Adv.* **10** (10), 105132.

NOGUEIRA, P.A.S., CAVALIERI, A.V.G., MARTINI, E., TOWNE, A., JORDAN, P. & EDGINGTON-MITCHELL, D. 2024 Guided-jet waves. *J. Fluid Mech.* **999**, A47.

NOGUEIRA, P.A.S., JAUNET, V., MANCINELLI, M., JORDAN, P. & EDGINGTON-MITCHELL, D. 2022 Closure mechanism of the A1 and A2 modes in jet screech. *J. Fluid Mech.* **936**, A10.

NOGUEIRA, P.A.S., JORDAN, P., JAUNET, V., CAVALIERI, A.V.G., TOWNE, A. & EDGINGTON-MITCHELL, D. 2022 Absolute instability in shock-containing jets. *J. Fluid Mech.* **930**, A10.

NORUM, T.D. 1983 Screech suppression in supersonic jets. *AIAA J.* **21** (2), 235–240.

OBERLEITHNER, K., SIEBER, M., NAYERI, C.N., PASCHEREIT, C.O., PETZ, C., HEGE, H.-C., NOACK, B.R. & WYGNANSKI, I. 2011 Three-dimensional coherent structures in a swirling jet undergoing vortex breakdown: stability analysis and empirical mode construction. *J. Fluid Mech.* **679**, 383–414.

PANDA, J. 1999 An experimental investigation of screech noise generation. *J. Fluid Mech* **378**, 71–96.

POWELL, A. 1953 On the mechanism of choked jet noise, proc. *Phys. Soc. B* **66** (12), 1039–1056.

POWELL, A. 1953 On the noise emanating from a two-dimensional jet above the critical pressure. *Aeronaut. Quart.* **4** (2), 103–122.

RAMAN, G. 1999 Supersonic jet screech: half-century from powell to the present. *J. Sound Vib.* **225** (3), 543–571.

RAMAN, G. & RICE, E.J. 1994 Instability modes excited by natural screech tones in a supersonic rectangular jet. *Phys. Fluids* **6** (12), 3999–4008.

RAMAN, G. & TAGHAVI, R. 1998 Coupling of twin rectangular supersonic jets. *J. Fluid Mech.* **354**, 123–146.

RODRÍGUEZ, D., STAVROPOULOS, M.N., NOGUEIRA, P.A.S., EDGINGTON-MITCHELL, D.M. & JORDAN, P. 2023 On the preferred flapping motion of round twin jets. *J. Fluid Mech.* **977**, A4.

SALEEM, M., KARNAM, A., RODRIGUEZ, O., LIU, J. & GUTMARK, E. 2023 Flow and acoustic fields investigation of noise reduction by micro vortex generators in supersonic nozzles. *Phys. Fluids* **35** (10), 106111.

SAMIMY, M., WEBB, N., ESFAHANI, A. & LEAHY, R. 2023 Perturbation-based active flow control in overexpanded to underexpanded supersonic rectangular twin jets. *J. Fluid Mech.* **959**, A13.

SCHMIDT, O.T. & COLONIUS, T. 2020 Guide to spectral proper orthogonal decomposition. *AIAA J.* **58** (3), 1023–1033.

SEMLITSCH, B., MALLA, B., GUTMARK, E.J. & MIHĂESCU, M. 2020 The generation mechanism of higher screech tone harmonics in supersonic jets. *J. Fluid Mech.* **893**, A9.

SETTLES, G.S. 2001 *Schlieren and Shadowgraph Techniques*. Springer.

SHEN, H. & TAM, C.K.W. 2002 Three-dimensional numerical simulation of the jet screech phenomenon. *AIAA J.* **40** (1), 33–41.

SIROVICH, L. 1987 Turbulence and the dynamics of coherent structures. I. Coherent structures. *Q. Appl. Math.* **45** (3), 561–571.

STAVROPOULOS, M.N., MARTINI, E., EDGINGTON-MITCHELL, D.M., WEIGHTMAN, J., JORDAN, P. & NOGUEIRA, P.A.S. 2024 On the behaviour of the upstream-travelling waves in merging twin-jet systems. *J. Fluid Mech.* **983**, A17.

TAM, C.K.W. 1995 Supersonic jet noise. *Annu. Rev. Fluid Mech.* **27** (1), 17–43.

TAM, C.K.W. & TANNA, H.K. 1982 Shock associated noise of supersonic jets from convergent-divergent nozzles. *J. Sound Vib.* **81** (3), 337–358.

TAM, C.K.W. & THIES, A.T. 1993 Instability of rectangular jets. *J. Fluid Mech.* **248**, 425–448.

TAM, C.K.W., VISWANATHAN, K., AHUJA, K.K. & PANDA, J. 2008 The sources of jet noise: experimental evidence. *J. Fluid Mech.* **615**, 253–292.

TOWNE, A., CAVALIERI, A.V.G., JORDAN, P., COLONIUS, T., SCHMIDT, O., JAUNET, V. & BRÈS, G.A. 2017 Acoustic resonance in the potential core of subsonic jets. *J. Fluid Mech.* **825**, 1113–1152.

WU, G.J., LELE, S.K. & JEUN, J. 2023 Analysis of resonance in jet screech with large-eddy simulations. arXiv:2304.00665

ZHANG, H., CHEN, Z., GUO, Z. & SUN, X. 2017 Characteristic behavior of shock pattern and primary vortex loop of a supersonic square jet. *Intl J. Heat Mass Transfer* **115**, 347–363.

ZHANG, H., CHEN, Z., JIANG, X. & GUO, Z. 2015 The initial flow characteristics of supersonic jets with different geometries. *Phys. Lett. A* **379** (18-19), 1256–1262.

ZILZ, D. & WLEZIEN, R. 1990 The sensitivity of near-field acoustics to the orientation of twin two-dimensional supersonic nozzles. In *26th Joint Propulsion Conference*. American Institute of Aeronautics and Astronautics.